Large-eddy simulations of turbulent flows using the high-order FR/CPR method

By

Yanan Li

Submitted to the Department of Aerospace Engineering and the
Graduate Faculty of the University of Kansas
in partial fulfillment of the requirements for the degree of
Doctor of Philosophy

Committee members

Dr. Z.J. Wang, Chairperson

Dr. Saeed Farokhi

Dr. Ray Taghavi

Dr. Xuemin Tu

Dr. Zhongquan Zheng

Date Defended: August 25, 2016

The Dissertation Committee for Yanan Li certifies
that this is the approved version of the following dissertation :

Large-eddy simulations of turbulent flows using the high-order FR/CPR method

Dr. Z.J. Wang, Chairperson

Date approved: August 25, 2016

Abstract

Large eddy simulation (LES) was originally proposed for simulating atmospheric flows and then has become one of the most successful methodologies for turbulence simulation for its good balance between accuracy and cost. In LES, energetic scales are resolved while the small equilibrium scales are modeled by the sub-grid scale(SGS) stress models. The resolution of the wide spectrum of the energetic scales is a big challenge for numerical methods. High-order methods are very promising in LES for its low dissipation and dispersion errors. For smooth turbulent flow, high-order methods have the potential to achieve high accuracy at lower cost than lower order methods. This thesis presents the investigation of the performance of different LES sub-grid scale stress (SGS) models with the high-order flux reconstruction or the correction procedure via reconstruction(FR/CPR) method. A mathematical analysis of scale similarity is conducted and presented as well. In addition, numerical schemes' behavior in nonlinear wave propagation is studied and presented.

The computationa of discontinuities, such as shocks, is another challenge to the numerical methods. In the simulation of shocks, non-physical oscillations can occur at the discontinuities and lead to divergence. The situation is worse for high-order methods. This thesis also presents a new flux limiter for the FR/CPR method. The new technique shows good properties, convergence for steady problems and accuracy preserving for vortex dominated flows. It is very promising in handling shock and turbulence interaction problems.

List of my Publications

[57] Yanan Li and Z. J. Wang. Evaluation of optimized CPR schemes for computational aeroacoustics benchmark problems. *AIAA Paper 2013-2689*, 2013.

[37] Y.Li and Z. J. Wang. A priori and a posteriori evaluations of sub-grid scale models with the burgers' equation. *AIAA Paper 2015-1283*, 2015.

[47] Z.J. Wang and Y.Li. An analysis of scale similarity and its implications for large eddy simulation. *Commun. Comput. Phys.*, 2016. Accepted.

[4] Y. Li and Z.J. Wang. A priori and a posteriori evaluations of sub-grid scale models with the burgers' equation. *Computers and Fluids*, 2016. Accepted.

[5] Z. J. Wang and Yanan Li. Recent progresses in large eddy simulations with the fr/cpr method. *ICCFD9-2016-149*, 2016.

Acknowledgements

I would like to take this opportunity to thank the people who made this thesis possible. First and foremost, I would like to express my most sincere gratitude to my adviser, Professor Z. J. Wang, for his generous advice, inspiring guidance and support throughout my graduate study. I would also like to thank my committee members, Professor Saeed Farokhi, Professor Xuemin Tu, Professor Zhongquan Zheng and Professor Ray Taghavi for their efforts, very useful comments and critical suggestions to this work.

I must express my gratitude to my group members, Lei Shi, Meilin Yu, Takanori Haga, Varun Vikas, Cheng Zhou, Ben Zimmerman, Zhaowe Duan, Jeremy Ims and Feilin Jia for all their support, insights and friendship throughout the years.

Finally, I would like to thank my parents for their continued support, understanding and encouragement.

Nomenclature

$\alpha_{j,f,l}$ the lifting constants

Δx_{DNS} the element size for DNS

Δx_i the length of element i

Δx_{LES} the element size for LES

Δ the filter width

δ_i the correction field on V_i

$\hat{u}$ the filtered solution

$\mid V_i \mid$ the volume of V_i

ν the constant viscosity

ν_{SGS} the SGS viscosity

Ω the non-dimensional wave number

Φ the limiting function

τ^{SGS} the SGS stress

$\vec{F}$ flux vector

A computation domain

$F^n(u_i)$ normal flux

F^n_{com} common Riemann flux

$G_\Delta(x, \xi)$ the low-pass filter

K degree of polynomial

k the frequency

L the resolved stress

L_j the shape function for solution point j

S_e the smoothness indicator of element e

S_f the face area

u state vector

u_i the approximate solution for element i

V_i discretized element

W weighting function

S_{ij} the rate of strain tensor

Contents

List of Figures

List of Tables

Chapter 1

Introduction

1.1 Background and Significance

For decades, Reynolds-averaged Navier-Stokes (RANS) methods have been used almost exclusively for the computational analysis of practical engineering turbulent flows in computational fluid dynamics (CFD). In RANS, all turbulent scales are modeled with a turbulence model. RANS-based techniques are successfully used in the industry for many problems. However, the behavior in the vortex dominated or massively separated flows are far from being satisfactory. On the other end, direct numerical simulation (DNS) methods resolve all turbulent scales. Without the influence of the turbulence modeling, it gives the whole spectrum of the turbulent flow. But DNS will still remain impractical for its high computational cost. Large-eddy simulation (LES) is a compromise of these two methods. In LES, large energetic scale motions are resolved while the small scale motions are taken care of by the SGS models. With the resolution of the important scales, the solution given by LES is expected to be more accurate than RANS, but, still affordable for problems of moderate Reynolds numbers.

Simulation of flow problems with discontinuities is another big challenge for CFD. Discontinuities are sudden changes in flow variables, which lead to non-physical oscillations in

numrical simulations. It ends in fuzzy simulation results or divergence. There are already many techniques to handle this issue, such as artificial viscosity, flux limiter, ENO/WENO schemes. However, for practical industry high Reynolds number transonic and supersonic problems, we have not found an ideal technique which is robust and also accuracy preserving. Research is still going on toward the ultimate technique.

The objective of this work is to develop a robust, accurate and efficient CFD tool for LES of transonic turbulence flow. It has the following properties: high-order methods for spatial discretization, appropriate SGS stress models and robust and accurate shock capturing techniques. In this section, we presents the motivation and a brief review of the background for these ideas.

1.1.1 High-Order CFD Methods

High-order methods mean that the error of the solution is proportional to a higher degree of the mesh cell size than the normal methods. High-order methods have received much attention for their ability to achieve high accuracy on a relatively low number of degrees of freedom. In the last two decades, many powerful high-order numerical methods have been developed, e.g. the spectral element method, discontinuous Galerkin (DG) method, spectral volume, spectral difference and the flux reconstruction or the correction procedure via reconstruction (FR/CPR) method. The advantage of high-order methods make it a good candidate in the computational fluid dynamics (CFD) for problems requiring a high-level accuracy, such as computational aero-acoustics and large eddy simulation of turbulent flows. In this work, we are using the FR/CPR method. The CPR method was recently developed in [1], and extended to simplex meshes in [2]. Further developments have been described in [3], [4]. The degrees-of-freedom (DOFs) are the state variables of a pre-defined nodal set named solution points (SPs), where the differential form of the governing equations is solved. As a results, explicit surface and volume integrals are avoided. The CPR formulation is among the most efficient discontinuous methods in terms of the number of operations.

1.1.2 Sub-grid Scale Stress Models

Large eddy simulations (LES) have been used in the computational of turbulent flows for decades because of the potential in resolving multiple turbulence scales. As a comparison, Reynolds-averaged Navier-Stokes(RANS) approaches model all scales of turbulence, while direct numerical simulation approaches resolve all turbulence scales. Although RANS models have been effective for many practical problems, they have difficulty handling complex massively separated unsteady flows. The use of DNS in computing high Reynolds number flows is also, for the forseeable future, limited by computing power [5]. LES is a compromise of the two approaches, and offers the best promise for vortex dominated separated flows. In LES, large scales and small scales are separated by a low-pass filter. The large scales are resolved while the effect of small scales is represented by an explicit sub-grid scale (SGS) stress model. Since small-scale motions are believed to be more universal, and thus easier to model than large scale ones, LES offers reasonable accuracy even for unsteady separated flows while requiring much less computer resources than DNS.

Many SGS models have been developed in the last four decades. We focuses on five of them: the static Smagorinsky model (SS)[6] [7], the dynamic Smagorinsky model (DS)[8], the scale-similarity model (SSM)[9], the mixed model (MM) [9] and the linear unified RANS-LES model (LUM) [10]. Among explicit models, the SS is a popular one because of its simplicity. The effect of the SGS stress upon the resolved scales is modeled as an eddy viscosity. The eddy viscosity is expressed in the mixing length form with a dimensionless empirical coefficient. However, it has been found that the empirical coefficient depends on the flow. It also adds too much dissipation to the large scale motions if we keep the coefficient the same as we approach wall boundaries. To resolve these deficiencies, the DS model was developed in [8]. In the DS model, the coefficient is calculated based on the Germano identity, which involves two levels of filtering and relates the SGS stress to the resolved stress. The coefficient is locally decided and no longer a prescribed constant, and it goes to zero as a wall boundary is approached. The DS model has been applied to a large

variety of flow simulations [11][12][13][14][15].

An alternative way to model the SGS stress is offered by the SSM [9]. As the name indicates, it assumes similarity between two scales of stresses, the resolved stress and the SGS stress. Numerical tests showed that energy accumulated at small scales with this model [16]. To remedy the problem, the DS was added to dissipate the energy, which led to the MM.

Recently, hybrid RANS-LES models have drawn much research interest. They combine RANS with LES so that in the near wall region, the RANS model is used, while LES is employed in the outer region. These models have demonstrated good accuracy with reasonable cost when compared to a pure LES approach. The linear unified RANS-LES model (LUM) was developed in [10]. In the present work, we also evaluate the LUM model.

Finally, we also consider the monotone integrated LES [17] or implicit LES (ILES) [18], in which no explicit SGS model is used. In ILES, the numerical algorithm has its numerical dissipation which serves as the SGS. The obvious advantage of ILES is its lower computational cost compared with the conventional SGS models.

Because of the disparate length scales in a turbulent flow, high-order methods are often preferred to compute the large scales because of their high accuracy. The present research studied the FR/CPR method together with the SGS models behavior in both 3D problems governed by the Navier-Stokes equations and a simplified 1D non-linear problem governed by the Burgers' equation.

1.1.3 Shock Capturing Techniques

Shock capturing techniques are highly demanded for the numerical simulation of high speed flows, such as supersonic and transonic flow over airfoils and turbine blades. Turbulence with shocks are even more widely seen in industry, such as helicopter/propeller fan blades, supersonic combustion ramjet engine. There are many existing methods to handle shocks, such as artificial viscosity[19] [20], flux limiter and ENO/WENO schemes[21] [22]. However,

the traditional shock capturing techniques are usually too dissipative, which destroy the vortex structures, or not robust enough for high Reynolds number problems.

A new convergent and accuracy preserving limiter is developed. By the introduction of a smoothness indicator, the over-limiting in the smooth regions is eliminated while enough limiting is added to the solution at the discontinuities.

1.2 Objectives of the Present Research

The main objective of this work is to develop a robust, accurate and efficient LES tool for transonic turbulent flow. In particular, the specific aims of this proposed research are identified as follows:

- Evaluate SGS models with 3D turbulent flows using FR/CPR method
- A priori and a posteriori evaluation of SGS models with Burgers' Equation and Euler Equations using FR/CPR method
- Mathematical analysis of the scale similarity
- Implement and evaluate existing shock capturing techniques
- Develop a new shock capturing flux limiter
- Demonstrate the accuracy and efficiency of LES with the high-order CPR method to aerodynamic flows and apply it to a wide range of engineering applications

1.3 Dissertation Organization

The rest of the thesis is organized as follows. In Chapter 2 the high-order CPR method used in this work is reviewed. An optimized CPR scheme (FOCPR) is presented and compared with the CPR scheme in the application of computational aero-acoustic problems. The a

priori and a posteriori evaluation and study of the SGS models are presented int Chapter 3, along with a mathematical analysis of a general scale similarity property. Chapter 4 describes the existing shock capturing technique and the new convergent accuracy preserving flux limiter we developed. Evaluation of the techniques are included int chapter 4 as well. Finally, conclusions and some possible future work are given in Chapter 5.

Chapter 2

The High-order CPR Method and An Optimization Scheme

High-order methods have received much attention for their ability to achieve high accuracy on relatively coarse meshes. In the last two decades, many powerful high-order numerical methods capable of handling unstructured meshes have been developed, e.g. the spectral element method, k-exact finite volume method, discontinuous Galerkin (DG) method, spectral volume, spectral difference and the correction procedure via reconstruction (CPR) methods.

The CPR method was recently developed in [1], and extended to simplex meshes in [2]. Further developments have been discribed in [3]. The degrees-of-freedom (DOFs) are the state variables of a pre-defined nodal set names solution points (SPs), where the differential form of the governing equations is solved. As a result, explicit surface and volume integrals are avoided. The CPR formulation is among the most efficient discontinuous methods in terms of the number of operations.

The stability and accuracy of the CPR method depend on the choice of the solution approximation and the weighting functions. Generally, the piecewise polynomial space is chosen for convection problems. However, they may not provide the best approximation for some PDEs and initial/boundary conditions. Here are some examples in the literature. The

locally divergence-free polynomial space was used in the DG method to solve the Maxwell equations and better results were achieved compared to the classical peicewise polynomial space in [23]. Exponential functions were proposed to solve singular perturbuation problems by Kadalbajoo and Patidar[24] and Reddy and Chakravarthy [25]. Non-polynomical spaces were used in the local essentially non-oscillatory (ENO) reconstruction for solving hyperbolic conservation laws in [26]. Exponential functions were also used near a boundary, and the trigonometric function for highly oscillatory problems, as shown by Yuan and Shu in [27].

Recently, a hybrid basis including both polynomial and Fourier terms was employed to resolve broadband wave propagation problems. It borrows the idea from the dispersion-relation-preserving (DRP) method [28] [29] [30] [31] [32] [33] to minimize both the dispersion and dissipation errors. Fourier terms were introduced to the basis of CPR because they have the ability to exactly represent waves at certain wave numbers, while monomials were employed to preserve a certain order of accuracy [34].

2.1 Review of the CPR Formulation

The CPR formulation can be derived form a weighted residual method by transforming the integral formulation into a differential one. The hyperbolic conservation law can be written as

$$\frac{\partial u}{\partial t} + \nabla \cdot \vec{F}(u) = 0, \tag{2.1}$$

with proper initial and boundary conditions, where u is the state vector, and $\vec{F}$ is the flux vector. The computation domain A is discretized into N non-overlapping elements $V_i, i = 1, ..., N$. Multiplying (2.1) with an arbitrary weighting function W and integrating over an element V_i, we obtain

$$\int_{V_i} (\frac{\partial u}{\partial t} + \nabla \cdot \vec{F}(u)) W dV = \int_{V_i} \frac{\partial u}{\partial t} W dV + \int_{\partial V_i} W \vec{F}(u) \cdot \vec{n} ds - \int_{V_i} \nabla W \cdot \vec{F}(u) dV = 0. \tag{2.2}$$

Let u_i be an approximate solution of the analytical solution u on element V_i. The solution is discontinuous across each element interface. On each element, the solution belongs to the space of polynomials of degree k or less, i.e. $u_i \in P^k(V_i)$. In addition, the numerical solution u_i is required to satisfy

$$\int_{V_i} \frac{\partial u_i}{\partial t} W dV + \int_{\partial V_i} W F^n_{com}(u_i, u_{i+}, \vec{n}) ds - \int_{V_i} \nabla W \cdot \vec{F}(u_i) dV = 0. \tag{2.3}$$

where $F^n_{com}(u_i, ui+, \vec{n})$ is the common Riemann flux, u_{i+} denotes the solution outside the current element V_i. Applying integration by parts again to the last term of the above LHS, we obtain

$$\int_{V_i} \frac{\partial u_i}{\partial t} W dV + \int_{V_i} W \nabla \cdot \vec{F}(u_i) dV + \int_{\partial V_i} W[F^n_{com}(u_i, u_{i+}, \vec{n}) - F^n(u_i)] dS = 0, \tag{2.4}$$

where $F^n(u_i)$ is the normal flux based on the current solution u_i. with the lifting operator, the boundary integral above is cast as a volume integral via the introduction of a correction field on V_i, $\delta_i \in P^k(V_i)$,

$$\int_{V_i} W \delta_i dV = \int_{\partial V_i} W[F^n] dS, \tag{2.5}$$

where $[F^n] = F^n_{com}(u_i, u_{i+}, \vec{n}) - F^n(u_i)$ is the normal flux difference. Substituting (2.5) into (2.4), we obtain

$$\int_{V_i} [\frac{\partial u_i}{\partial t} + \nabla \cdot \vec{F}(u_i) + \delta_i] W dV = 0. \tag{2.6}$$

(2.6) is equivalent to

$$\frac{\partial u_i}{\partial t} + \Pi(\nabla \cdot \vec{F}(u_i)) + \delta_i = 0, \tag{2.7}$$

where the $\Pi(\nabla \cdot \vec{F}(u_i))$ is a projection of $\nabla \cdot \vec{F}(u_i)$ to P^k. Next, let the DOFs be the solutions at a set of solution points (SPs) $\vec{r}_{i,j}$ (j varies from 1 to K). Then (2.7) holds true at the SPs, i.e,

$$\frac{\partial u_{i,j}}{\partial t} + \Pi_j(\nabla \cdot \vec{F}(u_{i,j})) + \delta_{i,j} = 0, \tag{2.8}$$

where $\Pi_j(\nabla \cdot \vec{F}(u_{i,j}))$ denotes the values of $\Pi(\nabla \cdot \vec{F}(u_i))$ at SP j. For linear triangles with straight edges, once the solution points and flux points are chosen, the correction at the SPs can be written as

$$\delta_{i,j} = \frac{1}{\mid V_i \mid} \sum_{f \in \partial V_i} \sum_{l} \alpha_{j,f,l} [F^n]_{f,l} S_f, \tag{2.9}$$

where $\alpha_{j,f,l}$ are lifting constants independent of the solution, S_f is the face area, $\mid V_i \mid$ is the volume of V_i. Substituting (2.9) into (2.8) we obtain the following CPR formulation

$$\frac{\partial u_{i,j}}{\partial t} + \Pi_j(\nabla \cdot \vec{F}(u_i)) + \frac{1}{\mid V_[i] \mid} \sum_{f \in \partial V_i} \sum_{l} \alpha_{j,f,l} [F^n]_{f,l} S_f = 0. \tag{2.10}$$

The 1D CPR formulation can be deduced from (2.10) as

$$\frac{\partial u_{i,j}}{\partial t} + \Pi_j(\frac{\partial F(u_i)}{\partial x}) + \frac{2}{\mid \Delta x_i \mid} (\alpha_{R,j} [F^n]_R + \alpha_{L,j} [F^n]_L) = 0, \tag{2.11}$$

where Δx_i is the length of element i, which has two interfaces, the left one and right one, with unit face areas and unit face normals of -1 and 1. It is often more convenient to transform the physical element in x to the standard element $[-1, 1]$ with coordinate ξ resulting in the following transformed equation

$$\frac{\partial u}{\partial t} + \xi_x \frac{\partial F(u)}{\partial \xi} = 0. \tag{2.12}$$

We consider the standard element $\xi \in [-1, 1]$. The approximation solution can be written as

$$u_i = \sum_{j=1}^{K} {}_j(\xi) u_{i,j}, \tag{2.13}$$

where L_j is the shape functions.

2.2 The Optimization Scheme

For high frequency wave propagation problems, the waves can be severely damped. Based on a Fourier analysis of the CPR method, it has large dissipation and dispersion errors for large wave numbers. The dispersion and the dissipation relations of the 4^{th} order CPR scheme are shown in Figure 2.1, where Ω is the non-dimensional wave number ($\Omega = w * \Delta x$). For the analysis, an upwind Riemann flux was used. In order to maximize the range of

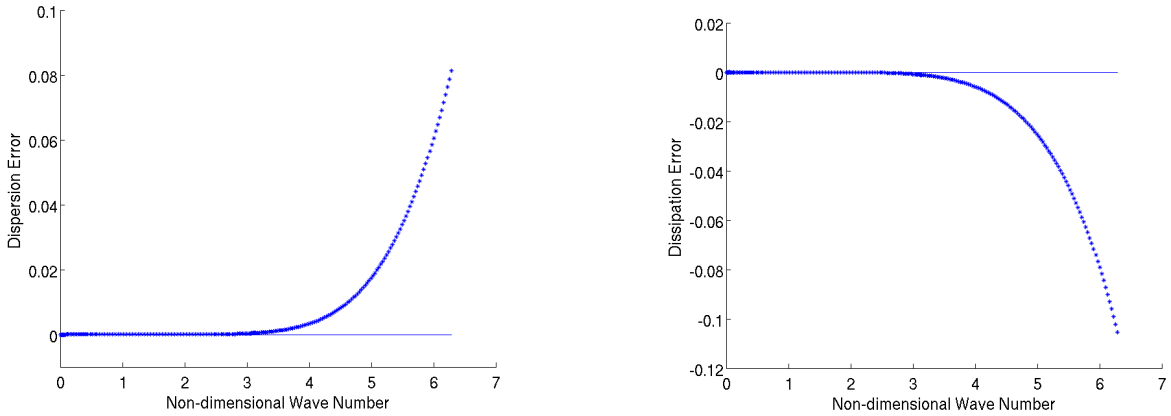

(a) (b)

Figure 2.1: Initial condition (left) and the initial energy spectrum (right)

waves that can be resolved accurately, the DRP method [35][36] was used to optimize the high-order finite difference schemes. For 1D problems, the approximation of the first order spatial derivative $\frac{\partial u}{\partial x}$ on a uniform grid fro a finite difference scheme is given by

$$(\frac{\partial u}{\partial x})_i \approx \frac{1}{\Delta x} \sum_{j=-N}^{M} a_j u(x_i + j\Delta x), \tag{2.14}$$

with M values to the right and N values to the left of the current point i. Rather than using the Taylor series expansion to determine the coefficients α_j, they are determined by requiring the Fourier transform of the finite difference scheme on the right hand side of (2.14) to be a close approximation of the partial derivative on the left hand side. The reader can refer to [35][36] for more details.

To achieve a similar benefit, in the CPR scheme, the Fourier components of certain frequencies are introduced into the basis functions. For each element, we define the following three spaces:polynomial, Fourier and hybrid

$$
\begin{aligned}
&B = span(1, \xi, \xi^2, \xi 3, ...), \\
&B = span(sin(\alpha 1 * \xi), cos(\alpha 1 * \xi), sin(\alpha 2 * \xi), cos(\alpha 2, *\xi)), \\
&B = span(1, \xi, \xi^2, \xi^3, ..., sin(\alpha 1 * \xi), cos(\alpha 1 * \xi), sin(\alpha 2 * \xi), cos(\alpha 2 * \xi), ...),
\end{aligned}
\tag{2.15}
$$

where $(\alpha 1, \alpha 2, ...)$ are free-parameters. The motivation to use the hybrid space instead of a polynomial space is to obtain a better approximation of broadband wave propagation, because the Fourier terms can exactly represent waves with certain non-dimensional wave numbers, Ω, and thus yield smaller dispersion and dissipation errors for relatively high frequency waves. At the same time, the monomials are used to achieve a certain order of accuracy with mesh refinement. The free-parameters are optimized to minimize both dispersion and dissipation errors over a specified range of wave numbers.

Because of the Fourier terms in the basis, the exact dispersion relation is satisfied at a certain Ω. Let's take a hybrid basis $B = (1, \xi, sin(2*\xi), cos(2*\xi))$ for instance. Its dispersion and dissipation relations are shown in 2.2. It is shown that this scheme gives no error at non-dimensional wave number $4(\Omega = \alpha * \Delta\xi = 2 * 2 = 4)$ and less error for wave numbers near 4 or larger than 4, compared with the polynomial basis. Since each element has 4 DOFs, this scheme has no spatial error if a wave has 6.28 DOFs, or the mesh satisfies 6.28 PPW (points per wave). This benefit can be obtained for any free parameter α. Obviously, if we choose a free parameter such that the non-dimensional wave numbers of a problem are all in the region where the FOCPR method has less error than the CPR method, we can obtain more accurate results without increasing the number of DOFs. It should e noted that the 1D Coefficients can be used for 2D problems on quadurilateral meshes because the two directions in each element can be treated as if they are decoupled.

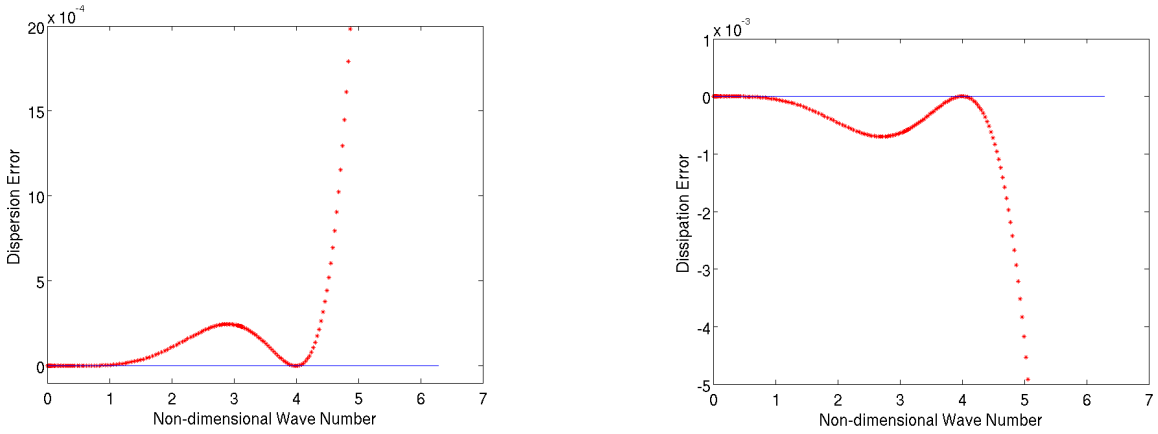

(a) (b)

Figure 2.2: Initial condition (left) and the initial energy spectrum (right)

2.3 Numerical Tests for CAA Problems

To evaluate the performance of the hybrid scheme, several computational aeroacoustic problems were tested using both the CPR and the FOCPR methods. In all the numerical evaluations in this dissertation, only the hybrid basis $B = 1, \xi, sin(\alpha * \xi), cos(\alpha * \xi)$ was compared with the 4^{th} order CPR method for the sake of simplicity.

2.3.1 1D Wave Propagation Test

The governing equation is given by

$$\frac{\partial u}{\partial t} + a\frac{\partial u}{\partial x} = 0, \tag{2.16}$$

with the following initial condition,

$$u(x, 0) = -sin(\pi x). \tag{2.17}$$

An explicit 3^{rd} order Runge-Kutta method was used in time marching. The computational domain is $[0, 20]$. The h refinement results are given in Figure 2.3. The benefit of the hybrid basis is clearly exhibited. It is shown that 2^{nd} order accuracy was achieved with the

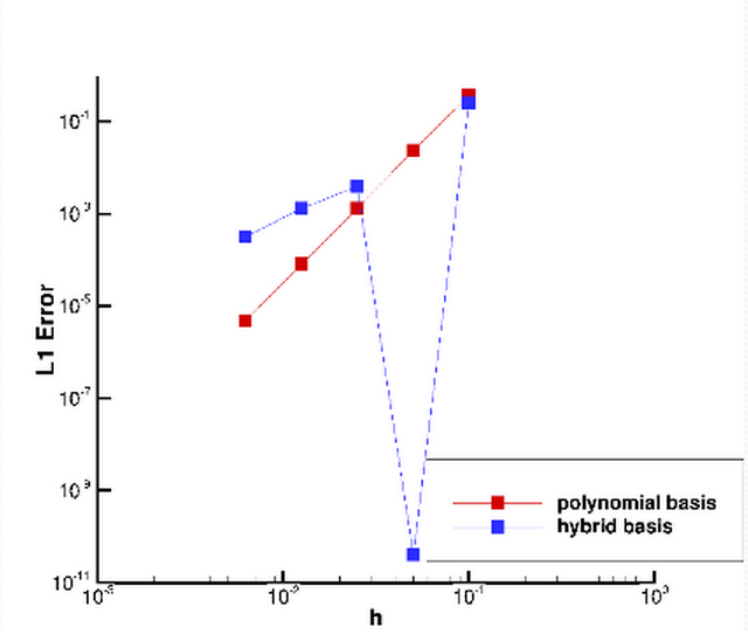

Figure 2.3: Error vs. mesh size with h refinement for schemes with 4 DOFs per element

h refinement for the FOCPR scheme, while 4^{th} order accuracy was achieved for the CPR scheme with a polynomial basis. When the points-per-wave (PPW) of the mesh matches the frequency at which the error of the FOCPR scheme is minimal, the spatial discretization is exact, thus the error is completely due to the time integration. This result agreed with the previous analysis. The monomial terms $(1, \xi)$ kept 2^{nd} order accuracy while the Fourier terms $(sin(\alpha * \xi), cos(\alpha * \xi))$ exactly represented the wave that matched the non-dimensional wave number of the scheme. It should be noted that, for mesh sizes that are smaller than the matching size, the error computed with the FOCPR method is larger than that computed with the CPR method.

2.3.2 1D Acoustic Wave Propagation

This 1D problem was computed on a 2D mesh, and the governing equations were the 2D Euler Equations. The computational domain, $[0, 20] \times [0, 1]$, was initialized with a uniform mean flow from left to right with Mach number $M = 0.5$. A perturbation of wave number

Figure 2.4: Pressure contours and mesh

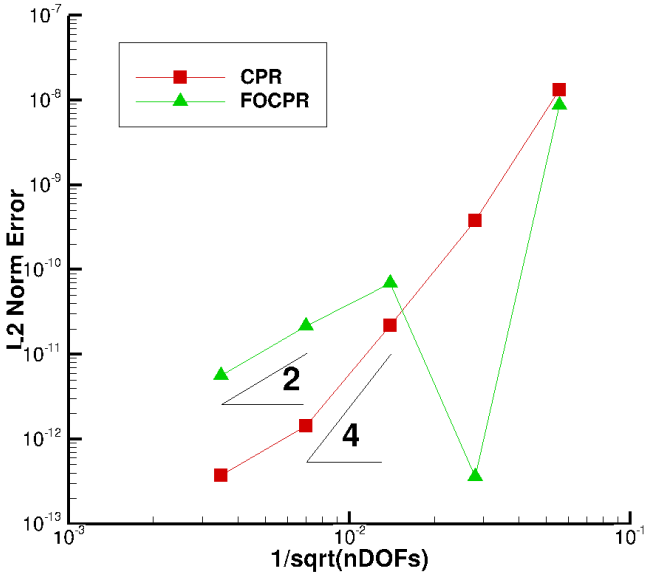

Figure 2.5: 1D wave propagation L2 norm error vs. h refinement

$k = 4$ and wave speed $\lambda = 1.5, \epsilon = 1.e{-}7$ was added from time $t = 0$. A uniform quadrilateral mesh was used. The equations were solved with both the CPR and the FOCPR methods in space and an explicit 3^{rd} order Runge-Kutta method in time. The analytic solutions are

$$\begin{aligned} p &= \tilde{p}\{1 + \epsilon cos[k(x - \lambda t)]\}, \\ \rho &= \tilde{\rho}\{1 + \frac{\epsilon}{\gamma} cos[k(x - \lambda t)]\}, \\ u &= \tilde{u}\{1 + \frac{\epsilon}{\gamma M} cos[k(x - \lambda t)]\}. \end{aligned} \tag{2.18}$$

The pressure contour at $t = 20$ is shown in Figure 2.4. The L2 norm error was calculated after 10 periods. The h refinement results are given in Figure 2.5. According to Figure 2.5, 2^{nd} order accuracy is achieved with the h refinement for the FOCPR scheme, while 4^{th} order

accuracy is achieved for the CPR scheme. We note that the lowest two points of the CPR scheme do not give 4^{th} order accuracy. It is becuase machine zero has been reached. When the PPW of the problem matches that of the FOCPR scheme, the error from the space discretization diminishes. Similar to the 1D linear wave propagation problem, we should note that the solutions of FOCPR scheme are not as accurate as that of the CPR method on smaller mesh sizes. The results of this numerical test confirm the benefit of the FOCPR method to 2D Euler Equations, which are usually solved in CAA problems.

2.3.3 Multi-geometry Scattering Problem

This case is the Category 2 Problem 1 from the Fourth CAA Workshop. It was the scattering of sound generated by a spatially distributed, axisymmetric, acoustic source from tow rigid circular cylinders. The governing equations were the unsteady Euler equations with a time dependent source term in the energy equation.

$$\frac{\partial Q}{\partial t} + \frac{\partial F}{\partial x} + \frac{\partial G}{\partial y} = S, \tag{2.19}$$

where Q is the vector of conserved variables, F and G are the inviscid flux vectors in x and y directions:

$$Q = \begin{bmatrix} \rho \\ \rho u \\ \rho v \\ E \end{bmatrix} \tag{2.20}$$

$$F = \begin{bmatrix} \rho u \\ \rho u^2 + p \\ \rho uv \\ u(E+p) \end{bmatrix} \tag{2.21}$$

$$G = \begin{bmatrix} \rho v \\ \rho uv \\ \rho v^2 + p \\ v(E+p) \end{bmatrix} \tag{2.22}$$

$$S = \begin{bmatrix} 0 \\ 0 \\ 0 \\ e^{-ln2\frac{x^2+y^2}{0.2^2}} sin(\omega t) \end{bmatrix} \tag{2.23}$$

The acoustic source used in this case had a transient term expressed in the following form

$$S = e^{-ln2\frac{x^2+y^2}{0.2^2}} sin(\omega t) f(t), f(t) = min(1, (\frac{t}{t_0})^3). \tag{2.24}$$

The following parameters were chosen in the present study: $w = 8\pi, t_0 = 4$. Since the configuration was symmetric, only the upper half of the physical domain was considered. The coarse mesh is shown in Figure 2.6 and it has 11359 cells. The resolution of the fine mesh is four times of the coarse mesh in both directions. The entire computational domain was a rectangle with length $a = 30$, width $b = 15$. The grid within $a_1 = 18, b_1 = 9$ was nearly uniform with a resolution of 6.28 points per wave. The mesh was coarsened in the outer region with and expansion factor of 1.1 to minimize the influence of reflection from the outer boundary. An explicit 3^{rd} order SSP Runge-Kutta method was used for time integration. The rms pressure was computed in the last 4 periods after force coefficients became periodic. The computed pressure field at a certain time is shown in Figure 2.7. The computed rms pressure along the center line is compared with the analytical solution in Figure 2.8. In this problem, the FOCPR scheme was optimized for waves at $4\pi = 12.5$ PPW to match the PPW for the cells near the cylinders. because the sound reflected from the cylinders affected the final solution very much. Figure 2.8 shows that the solution computed with

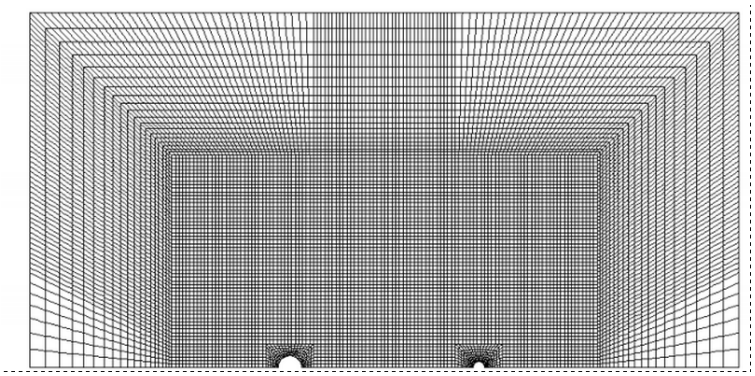

Figure 2.6: Computational grid for the two-cylinder scattering problem

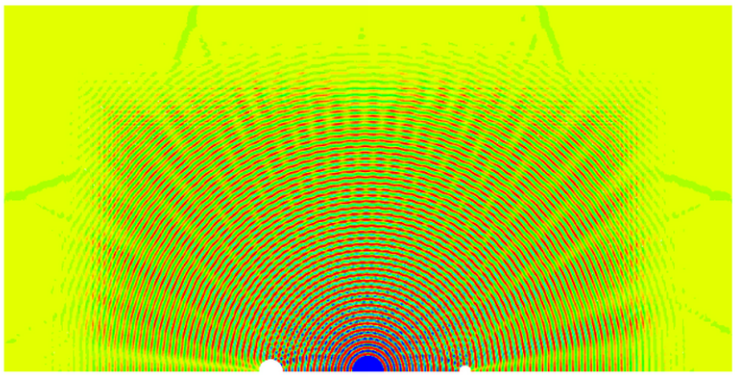

Figure 2.7: Computed pressure field

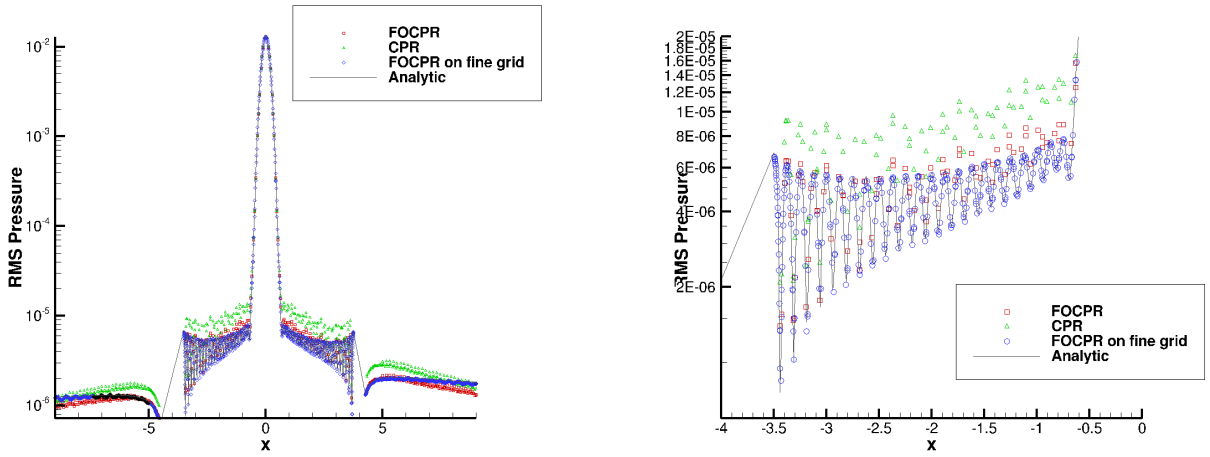

(a) (b)

Figure 2.8: Comparison of the computational and analytical RMS pressure along the center line

the FOCPR method converges to the analytic solution with mesh refinement. In fact, the solutions computed with both the CPR and FOCPR methods on the fine mesh agree with the analytical solution well. On the coarser mesh, the FOCPR method gave more accurate results than the CPR method. The performance of the FOCPR method was better than the CPR method on relatively coarser meshes. This can lead to a smaller number of DOFs for a given error-threshold for CAA problems.

2.3.4 Cascade-gust Interaction

This is a case from the Fourth CAA Workshop, Category 3 Problem 2. The two-dimensional geometry and the coarse and fine meshes are shown in Figure 2.9. The mesh is composed degree 4 elements generated with Gmsh. The coarse mesh has 2044 elements and the fine mesh has 8372 elements. The geometry is the unrolled section of a realistic three-dimensional fan outlet guide vane stator. It has a gap-to-chord ratio of $\frac{d}{c} = 2/3$ with the inflow and outflow planes located at $x_{\pm} = \pm\frac{3}{2}c$. The time-averaged inflow / outflow conditions are: inflow conditions, $\bar{P}_i = 1, \bar{T}_i = 1, \bar{\alpha}_i = 36^o$, outflow conditions, $\frac{\bar{P}_o}{\bar{P}_i} = 0.92$,where $\bar{P}_i$ and $\bar{T}_i$ are the normalized inflow plane mean stagnation pressure and mean stagnation temperature. $\bar{\alpha}_i$ is the mean flow angel and $\bar{P}_o$ the normalized outflow plane mean static pressure. The flow is assumed to be inviscid and isentropic throughout the domain.

The inflow gust (produced, say, by the wake of an upstream blade row) is given, at the inflow plane, by

$$\vec{u}_g'(y,t) = \{a_1 cos(k_y y - \omega t) + a_2 cos(2(k_y y - \omega t)) + a_3 cos(3(k_y y - \omega t))\}\hat{e}_\beta, \tag{2.25}$$

$$\hat{e}_\beta = cos(\beta)\hat{e}_x - sin(\beta)\hat{e}_y, \beta = 44^o, \tag{2.26}$$

$$\omega = \frac{3\pi}{4}, k_y = \frac{11\pi}{9}, a_1 = 5e-3, a_2 = 3e-3, a_3 = 7e-4 \tag{2.27}$$

where ω is the fundamental reduced frequency, k_y is the transverse wavenumber, and the a_i's are the gust harmonic amplitudes.

The steady solution was first obtained for the specified boundary conditions and then the three different frequencies of the inflow gust were added at the inflow plane, separately.

In the present simulation, a single passage was considered in the calculation for both the steady and unsteady situations in order to achieve the highest frequency. For the steady case, the flow was considered periodic at every passage, while for the unsteady perturbation case, a constant phase difference between adjacent blades was assumed. A brief discription of the treatment of the phase difference and phase-lagged boundary condition is given next.

The application of the phase-lagged boundary condition requires first storing the time variation of the fluid properties at the passage boundaries. They are then used to update the fluid properties associated with the other blades, which shifted in time with the phase of blade motion. Let us take the first component of the gust as an example. The width of the single passage is Δy, thus the phase difference θ between adjacent blades is $k_y * \Delta y$, which corresponds to a shift of $\frac{k_y * \Delta y}{\omega}$ in time. Let us define the interior solution at the boundary above the blade at any time to be $F_A(t)$, below the blade $f_B(t)$, and define the exterior boundary (ghost) condition at the boundary above the blade at any time to be $f_C(t)$, below the blade $f_D(t)$, respectively. $f_A(t)$ and $f_B(t)$ can be solved and stored. Then the exterior boundary (ghost) conditions can be obtained by

$$f_C(t) = f_B(t - \frac{k_y * \Delta y}{\omega}), f_D(t) = f_A(t - \frac{2\pi - k_y * \Delta y}{\omega}), \tag{2.28}$$

which are the prior solutions at the boundaries. It requires that $\frac{k_y \Delta y}{\omega}$ divided by the time step should be an integer. For the initial steps of computation, no prior information is available. During these steps, the boundaries are treated as being periodic. The errors introduced by this treatment increase the number of oscillations required for convergence.

Both the CPR and FOCPR methods were used to compute the steady solution on the

coarse and fine meshes. The free parameter of the FOCPR method here was chosen to be 2.0, which corresponds to 6.28 PPW. The steady pressure contours are shown in Figure 2.10.

For the unsteady perturbation, periodicity was achieved for all the simulations with different schemes. Figure 2.11 shows the history of the drag coefficient for the simulation with 3ω frequency computed with the 4^{th} order CPR method on the coarse mesh.THe axial velocity perturbation fields are shown in Figure 2.12. Table 2.1 shows the predicted amplitude of the unsteady blade surface pressure at three selected locations for each of the 3 frequencies computed with the FOCPR method on the coarse mesh. Table 2.2 shows the results computed with the 4^{th} order CPR method on the coarse mesh. Table 2.3 shows the results computed with the 6^{th} order CPR method on the coarse mesh and Table 2.4 shows the results computed with 4^{th} order CPR on the fine mesh. The results were given as SPL(dB)

$$SPL = 2 - log(\frac{p_{rms}}{p_{ref}}), \tag{2.29}$$

where $p_{ref} = 20\mu Pa$, p_{rms} was computed for 4 periods after periodicity was achieved. To demonstrate mesh and order independent solution convergence, the 4^{th} and 6^{th} order CPR schemes were used for the coarse mesh while the 4^{th} order CPR scheme was used on the fine mesh. The RMS pressures computed with the 6^{th} order CPR scheme on the coarse mesh differ less than 1% from those computed with the 4^{th} order CPR scheme on the fine mesh for all frequencies at all recorded locations, as shown in Table 2.3 2.4. Therefore, the fine mesh results are used as the true solution. The performance of the CPR and the FOCPR schemes are compared in Figure 2.13. the SPL(dB) values at $x = 0.25$ on the vane suction side for the gust component at frequency of 3ω were compared, because the highest frequency perturbation presented the most sever challenge for numerical methods.

It is shown that the SPLs computed with the FOCPR method on the coarse mesh are closer to the fine grid results than those computed with CPR method, demonstrating FOCPR's higher accuracy when the mesh barely has enough resolution to properly resolve

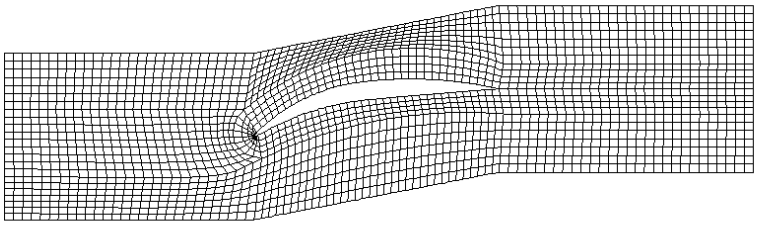

(a)

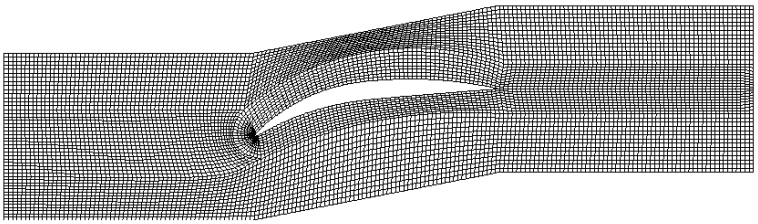

(b)

Figure 2.9: Computational grids for the cascade-gust interaction problem

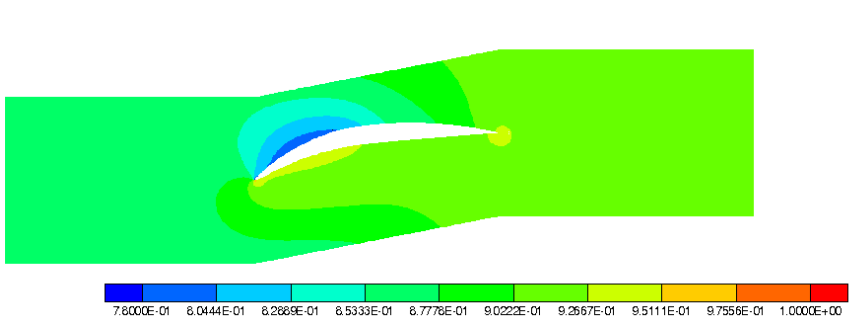

Figure 2.10: Pressure distribution for a steady flow over a cascade

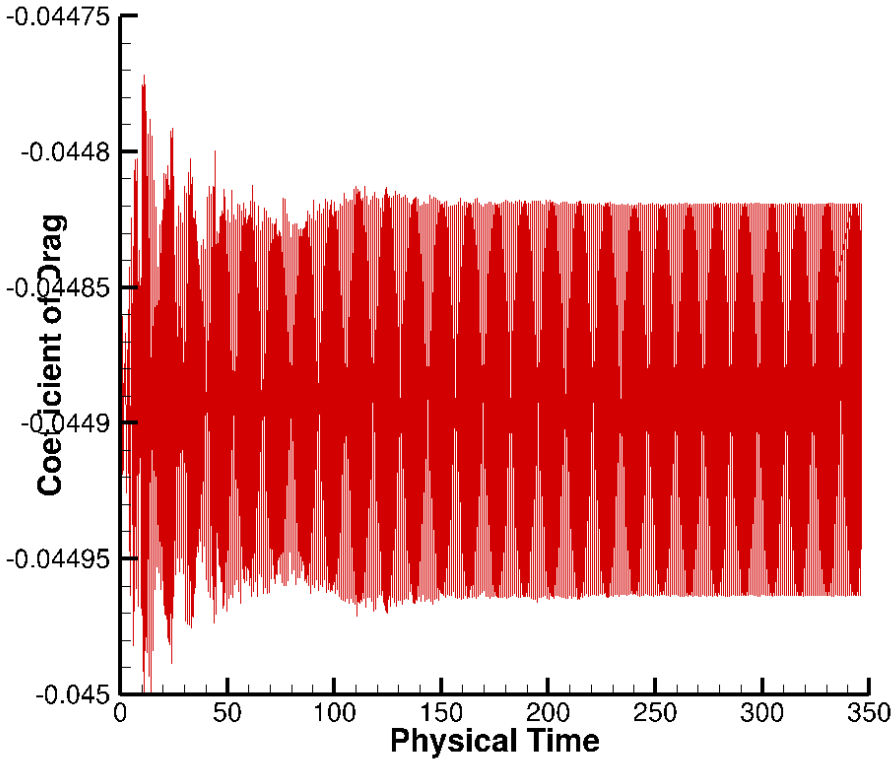

Figure 2.11: The history of drag coefficient

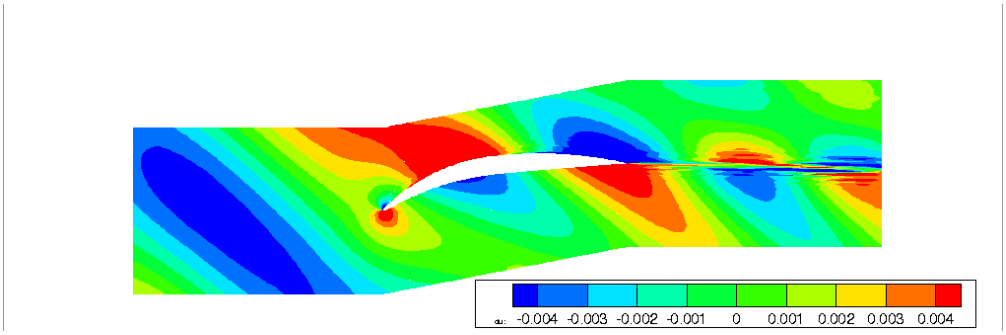

(a)

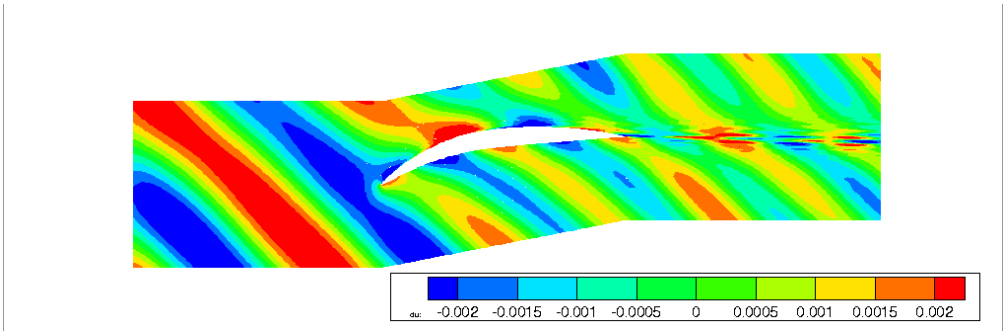

(b)

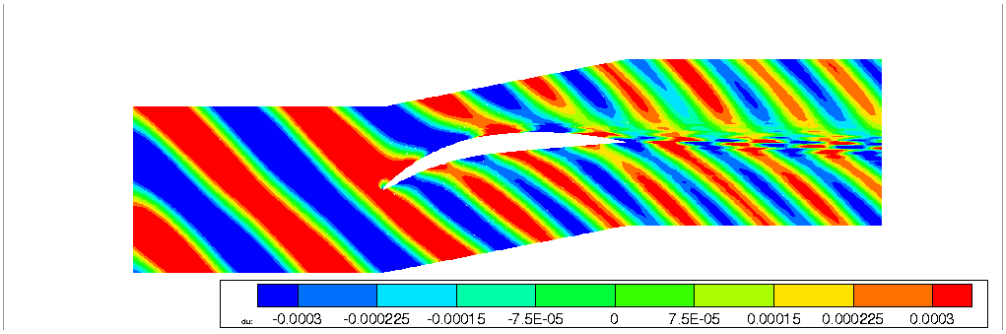

(c)

Figure 2.12: The axial velocity perturbation fields for (a) frequency ω (b) frequency 2ω (c) frequency 3ω using the FOCPR method on the coarse mesh

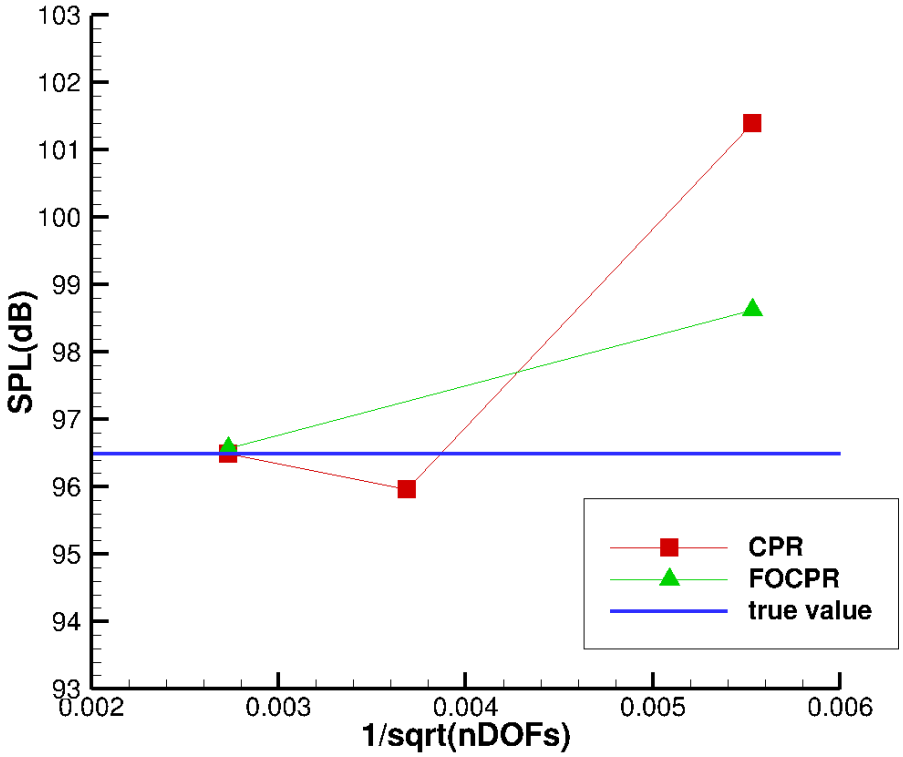

Figure 2.13: Acoustic pressure spectrum on the vane at $x = 0.25$, suction side vs. $1/sqrt(nDOFs)$ for frequency of 3ω

Table 2.1: Acoustic pressure spectrum on the vane using the FOCPR method on the coarse mesh

Frequence	Suction Side SPL(dB)			Pressure Side SPL(dB)		
	$x/c = -0.25$	$x/c = 0.00$	$x/c = 0.25$	$x/c = -0.25$	$x/c = 0.00$	$x/c = 0.25$
ω	141.897	141.763	142.166	139.277	142.508	141.294
2ω	132.019	129.662	118.348	126.329	127.595	116.29
3ω	110.349	116.984	98.630	115.922	112.712	108.951

Table 2.2: Acoustic pressure spectrum on the vane using the 4^{th} order CPR method on the coarse mesh

Frequence	Suction Side SPL(dB)			Pressure Side SPL(dB)		
	$x/c = -0.25$	$x/c = 0.00$	$x/c = 0.25$	$x/c = -0.25$	$x/c = 0.00$	$x/c = 0.25$
ω	141.763	141.66	142.102	139.137	142.423	141.253
2ω	131.946	129.761	119.081	126.209	127.57	116.926
3ω	110.286	116.864	101.4	115.896	112.694	109.375

high frequency waves. Note that on the fine mesh, the SPLs computed with both the CPR and FOCPR schemes are very similar, indicating convergence independent of the numerical method. From Figure 2.9, it is obvious that the elements are very small at the leading edge and the trailing edge to satisfy the geometry resolution requirement. But the elements at the inlet, outlet, top and bottom boundaries are much larger to reduce the number of DOFs. The non-dimensional wave numbers vary significantly from one region of the mesh to another. Some of the wave numbers are located outside the region where the FOCPR method has smaller error than the CPR method. As a result, the benefit from the FOCPR scheme was not as obvious.

2.3.5 Summary of Comparison Between CPR And FOCPR Schemes

The FOCPR method was developed to improve the resolution of the CPR formulation for broadband waves. In the numerical evaluation of the 1D linear wave propagation, the

Table 2.3: Acoustic pressure spectrum on the vane using the 6^{th} order CPR method on the coarse mesh

Frequence	Suction Side SPL(dB)			Pressure Side SPL(dB)		
	$x/c = -0.25$	$x/c = 0.00$	$x/c = 0.25$	$x/c = -0.25$	$x/c = 0.00$	$x/c = 0.25$
ω	142.165	141.94	142.214	139.647	142.742	141.417
2ω	132.076	129.456	118.035	126.415	127.522	113.99
3ω	111.488	117.81	95.968	115.586	112.798	108.451

Table 2.4: Acoustic pressure spectrum on the vane using the 4^{th} order CPR method on the fine mesh

Frequence	Suction Side SPL(dB)			Pressure Side SPL(dB)		
	$x/c = -0.25$	$x/c = 0.00$	$x/c = 0.25$	$x/c = -0.25$	$x/c = 0.00$	$x/c = 0.25$
ω	142.203	141.967	142.225	139.6807	142.763	141.425
2ω	132.096	129.432	117.803	126.547	127.667	113.801
3ω	111.904	118.286	96.493	115.848	113.281	107.7131

FOCPR method was able to exactly represent the wave whose non-dimensional wavenumber matched the scheme's non-dimensional wavenumber and achieved 2^{nd} order accuracy with mesh refinement. In the 1D wave propagation problem using the 2D Euler equations, the FOCPR method also showed similar benefits. For both benchmark problems from the 4^{th} Computational Aeroacoustic (CAA) Workshop when the mesh resolution is barely enough to resolve the high-frequency components, the FOCPR method shows a clear advantage in accuracy on the coarse mesh. Once the mesh was refined, the benefit was not as obvious becuase int eh limit of diminishing mesh size, the CPR scheme is always ore accurate by design. As a result, for problems with widely varying non-dimensional wave numbers, the advantage of the FOCPR method may be limited.

Chapter 3

Large Eddy Simulation Using the CPR Method

3.1 A Priori and a Posteriori Evaluations of Sub-grid Scale Models with the Burgers' Equation

The LES of decaying homogeneous isotropic turbulence with the FR/CPR method was conducted recently [37]. The ILES approach always produces better results than the static or dynamic Smagorinsky model through comparison with the DNS results. Figure 3.1 shows the comparison of the normalized dissipation rate. Figure 3.2 shows the energy spectra at two different times. From both figures, we see that on a given coarse mesh, ILES yields more accurate results than the LES with the Smagorinsky models.

To understand the reason, all the SGS models are evaluated with the one dimensional Burgers' equation rather than the full Navier-Stokes equations. The 1D Burgers' equation is not a model for the 3D turbulence, but it is still a good one for assessing the SGS models because of its nonlinear convection term. We initialize the simulations mimicking a typical turbulence energy spectrum in the Fourier space with random phase angles. The FR/CPR method is used to discretize the Burgers' equation and the explicit three-stage Runge-Kutta

scheme is employed for time integration.

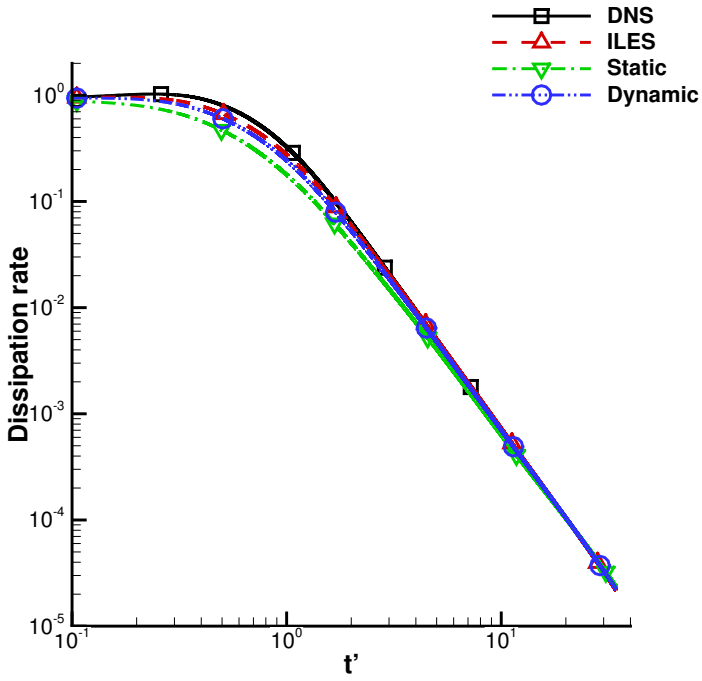

Figure 3.1: Normalized dissipation rate

3.1.1 Governing Equation and SGS Models

The governing equations for three dimensional turbulent flows are the three dimensional Navier-Stokes equations. As a simpler counterpart, we consider the one dimensional Burgers' equation,

$$\frac{\partial u}{\partial t} + u\frac{\partial u}{\partial x} = \nu\frac{\partial^2 u}{\partial^2 x}, x \in [-1, 1], \tag{3.1}$$

where u is the state variable such as velocity, ν is a constant viscosity. In the present study, $\nu = 8E - 05$ is chosen to imitate a high Reynolds number flow problem. To derive the LES governing equation, we apply a low-pass spatial filter, $G_\Delta(x, \xi)$ satisfying the following conservative property

$$\int_{-\infty}^{\infty} G_\Delta(x, \xi)d\xi = 1, \tag{3.2}$$

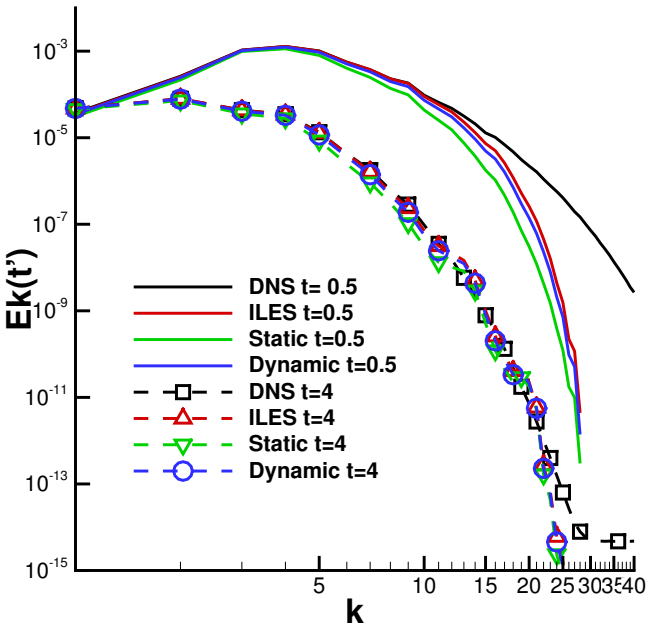

Figure 3.2: The energy spectra at non-dimensional time 0.25 and 4

where Δ denotes the filter width. A typical filter, the box filter, is defined below,

$$G_\Delta(x,\xi) = \begin{cases} \frac{1}{\Delta} & |x-\xi| \leq \frac{\Delta}{2}, \\ 0 & otherwise \end{cases} \tag{3.3}$$

The filtering process is defined mathematically in the physical space as a convolution product. The filtered variable $\hat{\phi}(x,t)$ of a space-time variable $\phi(x,t)$ in 1D is defined as

$$\hat{\phi}(x,t) = \int_{-\infty}^{\infty} G(x,\xi)\phi(x,t)d\xi. \tag{3.4}$$

The filtering process is linear, i.e. $\phi \hat{+} \varphi = \hat{\phi} + \hat{\varphi}$. If the filter width is constant, the differential and the filter operators commute, i.e. $\frac{\partial\hat{\phi}}{\partial x} = \frac{\partial\hat{\phi}}{\partial x}$. In the present study, all the filtering processes are done with the box filter. After applying the filter to Eq. (3.1), we

obtain

$$\frac{\partial \hat{u}}{\partial t} + \hat{u}\frac{\partial \hat{u}}{\partial x} = \nu \frac{\partial^2 \hat{u}}{\partial^2 x} - \frac{\partial(\frac{1}{2}\hat{u}u - \frac{1}{2}\hat{u}\hat{u})}{\partial x}. \tag{3.5}$$

The unclosed term arises due to the filtering of the nonlinear convection term

$$\tau^{SGS} = \frac{1}{2}\hat{u}u - \frac{1}{2}\hat{u}\hat{u}. \tag{3.6}$$

This is the SGS of the Burgers' equation. SGS models act as the closure of the governing equation. In this section we review some of the ideas and translate them to work for the one dimensional Burgers' equation.

3.1.1.1 Static Smagorinsky Model

The SS is in the eddy viscosity form. For 3D incompressible flow, the SGS stress is defined as,

$$\tau_{ij}^{SGS} = -2\nu_{SGS}\hat{S_{ij}}, \tag{3.7}$$

where $\hat{S}_{i,j}$ is the resolved rate of strain tensor, and

$$\hat{S}_{i,j} = \frac{1}{2}(\partial_i \hat{u}_j + \partial_j \hat{u}_i). \tag{3.8}$$

The SGS viscosity, ν_{SGS} is modeled following the mixing length idea

$$\nu_{SGS} = (c_s\Delta)^2\sqrt{2|\hat{S}|^2}, \tag{3.9}$$

where $|\hat{S}|^2 = \hat{S}_{ij}\hat{S}_{ji}$, c_s is the prescribed coefficient. By comparing the mean SGS dissipation from DNS data and the modeled SGS dissipation, c_s can be determined. Lilly used this procedure for isotropic turbulence to obtain $c_s = 0.16$. The SS was described by Moin and Kim [38], Rogallo and Moin [39], Lesieur and Metais [40] and Pope [41]. The deficiency of this model first showed up in the comparison of the modeled SGS stress and the true SGS

stress computed from the DNS solution by Clark et al. [42], McMillan and Ferziger [43], and Bardina et al. [9]. The comparisons imply that the model does not capture the SGS adequately. In [16], Meneveau et al. gave an explanation of this problem. Another weakness of this model is that it gives non-zero eddy viscosity in laminar-flow regions. Therefore a wall function is needed to damp the SGS viscosity in a wall-bounded flow. Next, we derive its 1D formulation. The rate of strain in 1D is

$$\nu_{SGS} = (c_s\Delta)^2|\partial_x\hat{u}|. \tag{3.10}$$

Therefore the SGS stress becomes

$$\tau^{SGS} = -\nu_{SGS}\hat{S} \tag{3.11}$$

3.1.1.2 Dynamic Smagorinsky Model

The coefficient, c_s, in SS is prescribed. However, it is found empirically that c_s depends on the flow, being 0.1 for plane channel flow and 0.2 for isotropic turbulence [17]. The DS makes it a variable spatially and temporally. It introduces a test filter to the resolved scales and uses the assumption of scale invariance to compute the model coefficient. As the model for three dimensional turbulence is readily available, we derive it for the 1D Burgers' equation next.

Following Eq. /eqnrefe:filtered burgers, we consider the 2^{nd} filter with width $\hat{\Delta}$, defined as $\hat{\Delta} = \gamma\Delta$. By applying this filter to the SGS stress, we obtain

$$\hat{\tau}^{SGS} = \frac{1}{2}\widetilde{u\hat{u}} - \frac{1}{2}\widetilde{\hat{u}\hat{u}}. \tag{3.12}$$

By applying the filter to the LES solution, we obtain the resolved stress,

$$L = \frac{1}{2}\widetilde{\hat{u}\hat{u}} - \frac{1}{2}\tilde{\hat{u}}\tilde{\hat{u}}. \tag{3.13}$$

The Germano identity can be written as

$$T = \tilde{\tau}^{SGS} + L \tag{3.14}$$

where $T = \frac{1}{2}\widetilde{u\tilde{u}} - \frac{1}{2}\tilde{\hat{u}}\tilde{\hat{u}}$. We apply the SS to both T and τ and assume they share the same coefficient, c_s,

$$-(c_s\tilde{\Delta})^2|\partial_x\tilde{\hat{u}}|\partial_x\tilde{\hat{u}} = -(c_s\Delta)^2|\partial_x\widetilde{\hat{u}}|\partial_x\widetilde{\hat{u}u} + L. \tag{3.15}$$

We define

$$M = \Delta^2|\partial_x\widetilde{\hat{u}}|\partial_x\widetilde{\hat{u}u} - \tilde{\Delta}^2|\partial_x\tilde{\hat{u}}|\partial_x\tilde{\hat{u}}. \tag{3.16}$$

Thus $c_s^2 = \frac{L}{M}$. It is assumed that c_s is spatially uniform so that it can be extracted from the test-filtering operation (Ghosal et al 1995)[44]. In the 1D test, we take the most common choice of $\gamma = 2$. In three dimensions, this is an over-determined system. To minimize the square error, Lilly used the following approach

$$c_s^2 = \frac{\langle L_{ij}M_{ij}\rangle}{\langle M_{ij}M_{ij}\rangle}, \tag{3.17}$$

where $\langle\cdot\rangle$ means averaging along the homogeneous direction. The DS gives a highly variable eddy viscosity field [8] including negative values which makes the simulation unstable. Averaging over homogeneous directions was used by Germano et al. [8] to prevent this problem. Ghosal et al. [44] showed that this procedure minimizes the total error in the homogeneous region over which the averaging is performed. With these modifications, the eddy viscosity still can be negative. So the value of c_s^2 is clipped to be non-negative. In 1D, we don't have these problems. Thus we don't use a least square averaging operation. But we still require c_s^2 to be non-negative.

3.1.1.3 Scale-Similarity model

The SSM was first introduced by Bardina et al. [9]. It assumes scale invariance between the computable stress L and the SGS stress τ^{SGS}. This assumption was verified with empirical band pass-filtered PIV measurements by Liu et al. [45]. It suggests that is similar to a stress constructed from the resolved scales,

$$\tau^{SGS} = c_{ssm} L, \tag{3.18}$$

where L s the resolved stress, which is given in Eq. /eqnrefe:resolved stress. Many different second filter widths were suggested by various researchers. The Bardina's original model uses the same filter width for the two filters, i.e. $\Delta = \hat{\Delta}$ and $\gamma = 1$. Liu et al used $\gamma = 2$ and Akhavan et al use $\gamma = \frac{4}{3}$ [46]. The coefficient c_{ssm} is empirical and found to be close to 1. In the 1D test, c_{ssm} is adjusted to be 0.25 with , based on an analysis performed in [47]. In [9], the true and modeled stresses showed a high degree of correlation in Bardina et al's a priori tests, and the SSM allowed for energy backscatter. However, this model was found to be not sufficiently dissipative. Energy accumulated at small scales and finally led to numerical instability. In the present study, we will duplicate this result with a non-dissipative numerical scheme, and will show that the phenomenon does not occur with the dissipative FR/CPR method.

3.1.1.4 Mixed Model

To resolve the above-mentioned problem of the SSM, the DS is included in the formulation to add extra dissipation. In three dimensions, the mixed model (MM) is

$$\tau_{ij}^{SGS} = c_{ssm} L_{ij} - 2\nu_{SGS} \hat{S}_{ij}. \tag{3.19}$$

Liu et al. showed that the magnitude of the similarity term is much larger than that of the dissipative DS term. Hence, the high correlation of the SSM is not degraded by the extra viscosity. Zang et al. [48] used this model for recirculating flows with $\gamma = 1$. Wu and Squires applied this model successfully with Lagrangian averaging in simulations of 3D boundary layers [49]. There are dynamic ways to determine c_{ssm} as well. Vreman et al [50] proposed a two-parameter dynamic MM in which c_s and c_{ssm} are both calculated dynamically with $\gamma = 1$. In the present one dimensional study, the values $c_{ssm} = 0.25$ and $\gamma = 2$ are used. The SGS stress is defined as

$$\tau = c_{ssm}(\frac{1}{2}\tilde{\hat{u}\hat{u}} - \frac{1}{2}\tilde{\hat{u}}\tilde{\hat{u}}) - \nu_{SGS}\hat{S}. \tag{3.20}$$

As will be shown later, the numerical instability of the SSM model is not a problem for numerical schemes with embedded numerical dissipation. The study will be described and discussed in Section 4.

3.1.1.5 Linear Unified RANS-LES Model

The wall-bounded turbulent flows at high Reynolds number are a significant challenge for LES. The near wall region requires a high resolution grid to resolve the small energetic scales. The linear unified RANS-LES model (LUM) combines RANS with LES to solve this problem. The model equations for incompressible flows are

$$\begin{cases} \dfrac{\tilde{D}\tilde{U}_i}{\tilde{D}t} = -\dfrac{\partial(\frac{\langle p\rangle}{\rho} + \frac{2k_t}{3})}{\partial x_i} + 2\dfrac{\partial(\nu+\nu_t)\tilde{S}_{ik}}{\partial x_k} & \text{(3.21a)} \\ \dfrac{\tilde{D}k_t}{\tilde{D}t} = -\dfrac{\partial((\nu+\nu_t)\frac{\partial k_t}{\partial x_i})}{\partial x_i} + \nu_t S^2 - 2\dfrac{(1-c_0)k_t}{\tau_L} & \text{(3.21b)} \\ \dfrac{\tilde{D}\omega}{\tilde{D}t} = C_{\omega 1}\dfrac{\omega}{k}nu_t S^2 - \dfrac{C_{\omega 2}}{C_k k}\omega^2 + \dfrac{\partial((\nu+\frac{\nu_t}{\sigma_{omega}})\frac{\partial\omega}{partialx_j})}{\partial x_j} + \dfrac{C_\omega}{k}(\nu+\nu_t)\dfrac{\partial k_t}{\partial x_j}\dfrac{\partial\omega}{\partial x_j} & \text{(3.21c)} \end{cases}$$

where $C_{\omega 1}, C_{\omega 2}, C_\omega, C_k, c_0 and \sigma_\omega$ are all model constants, $\hat{U}_i$ is the filtered velocity, k_t is the turbulent kinetic energy, ω is the specific dissipation, τ_L is the time scale and ν_t is the

modeled viscosity. In this work, we only focus on the LES aspect of the model. Therefore τ_L is calculated with $\tau_L = l_{ast}\Delta/k^{\frac{1}{2}}$, where $l_* = \frac{1}{3}$. In summary, for the one-dimensional Burgers' equation, we solve

$$\begin{cases} \dfrac{\hat{D}\hat{u}}{\hat{D}t} = \dfrac{\partial(\nu+\nu_t)\frac{\partial\hat{u}}{\partial x}}{\partial x} & \text{(3.22a)} \\ \dfrac{\hat{D}k_t}{\hat{D}t} = -\dfrac{\partial((\nu+\nu_t)\frac{\partial k_t}{\partial x})}{\partial x} + 2\nu_t(\dfrac{\partial\hat{u}}{\partial x})^2 - 2\dfrac{(1-c_0)k_t}{\tau_L} & \text{(3.22b)} \end{cases}$$

where $\nu_t = \frac{k_t\tau_L}{3}$, $\tau_L = l_*\Delta/k_t^{\frac{1}{2}}$.

3.1.2 High-order FR/CPR method

To give a complete picture of the LES, in this section, we briefly review the FR/CPR method's formula for the 1D Burgers' equation. Huynh [1] developed a high-order FR/CPR formulation, which was later employed for the Navier-Stokes equations on hybrid 3D meshes [51]. It has been used for 1D, 2D and 3D laminar and turbulent flows. Validations and successful applications can be found in [52] [53] [54] [55] [56] [57]. In this study, we apply the 3^{rd} order FR/CPR scheme to the 1D Burgers' equation and evaluate its performance with various SGS models. The FR/CPR formulation for the inviscid 1D Burgers' equation is given as

$$\frac{\partial u_{i,j}}{\partial t} + \Pi(\frac{\partial F(u_i)}{\partial x}) + \frac{1}{\Delta x_i}(\alpha_{R,j}[F^n]_i + 1/2\alpha_{L,j}[F^n]_i - 1/2) = 0, \tag{3.23}$$

where $u_{i,j}$ is the solution at solution point j of element i, u_i is the solution polynomial for element i, $\Pi(\frac{\partial F(u_i)}{\partial x})$ denotes the projected flux derivative at the solution point, Δx_i is the length of element i, $[F^n]_{i+1/2}$ and $[F^n]_{i-1/2}$ are the differences between the local flux and the common Riemann flux at the right and left interfaces of element i, $\alpha_{R,j}$ and $\alpha_{L,j}$ are the correction coefficients independent of the solution variables. For the viscous term on the right hand side of Burgers' equation, we follow the BR2 approach [58]. The 1D version is

described below. First we introduce a new variable $R = \frac{\partial u}{\partial x}$. The corrected gradient is then

$$R_{i,j} = \frac{\partial u_{i,j}}{\partial x} + \frac{1}{\Delta x_i}(\alpha_{R,j}[u^{com} - u_i]_{i+1/2} + \alpha_{L,j}[u^{com} - u_i]_{i-1/2}), \tag{3.24}$$

where $[u^{com}]_{i+1/2}$ and $[u^{com}]_{i-1/2}$ are the common solutions at interfaces, $[u_i]_{i+1/2}$ and $[u_i]_{i-1/2}$ are the solutions from element i at the interfaces. The common solution is defined as

$$u^{com}_{i+1/2} = \frac{u^-_{i+1/2} + u^+_{i+1/2}}{2}, \tag{3.25}$$

where $u^-_{i+1/2} = [u_i]_{i+1/2}$ and $u^+_{i+1/2} = [u_{i+1}]_{i+1/2}$ are the solutions at the left and right sides of interface $i + 1/2$. Next, the viscous flux, $F^\nu = \nu\frac{\partial u}{\partial x}$, at solution points can be calculated by

$$F^\nu_{i,j} = F^\nu(R_{i,j}). \tag{3.26}$$

Then $\frac{\partial F^\nu}{\partial x}$ can be obtained by using the Lagrange polynomial approach. The common viscous flux at the interface is needed to correct $\frac{\partial F^\nu}{\partial x}$ at solution points,

$$F^{\nu,com}_{i+1/2} = \nu(\frac{\partial u}{\partial x})^{com}_{i+1/2}. \tag{3.27}$$

For the common gradient,

$$(\frac{\partial u}{\partial x})^{com}_{i+1/2} = \frac{1}{2}((\frac{\partial u}{\partial x})^-_{i+1/2} + r^-_{i+1/2} + (\frac{\partial u}{\partial x})^+_{i+1/2} + r^+_{i+1/2}). \tag{3.28}$$

where $(\frac{\partial u}{\partial x})^-_{i+1/2}$ and $(\frac{\partial u}{\lceil}\partial x])^+_{i+1/2}$ are the gradients of the solution of the left and right cells with no correction, $r^-_{i+1/2}$ and $r^+_{i+1/2}$ are the corrections to the gradients due to the common solution at the interface. More specifically, the corrections are,

$$r^-_{i+1/2} = \frac{1}{\Delta x_i}(\alpha^-[u^{com} - u^-]_{i+1/2}), \tag{3.29}$$

$$r^{+}_{i+1/2} = \frac{1}{\Delta x_{i+1}}(\alpha^{+}[u_{com} - u^{+}]_{i+1/2}), \tag{3.30}$$

where α^{-} and α^{+} are the interface correction coefficients.

3.1.3 Temporal Discretization

The explicit SSP three-stage 3^{rd} order Runge-Kutta scheme [59] is used as the temporal discretization. Here we give a brief description. Rewrite the discretized Burgers' equation as

$$\frac{\partial U}{\partial t} = Res(U), U(t_0) = U_0, \tag{3.31}$$

where $Res(U)$ is a function of solution U and t. Given solution U^n, we obtain solution U^{n+1} using

$$U^{(1)} = U^n + \Delta t Res(U^n), \tag{3.32}$$

$$U^{(2)} = \frac{3}{4}U^n + \frac{1}{4}U^{(1)} + \frac{1}{4}\Delta t Res(U^{(1)}), \tag{3.33}$$

$$U^{n+1} = \frac{1}{3}U^n + \frac{2}{3}U^{(2)} + \frac{2}{3}\Delta t Res(U^{(2)}). \tag{3.34}$$

3.1.4 Initial and Boundary Conditions for 1D Burgers' Equation

To imitate turbulence, the initial energy spectrum is given in the Fourier space k. In the present work, the following initial spectrum is used

$$E_0(k) = \begin{cases} A5^{-\frac{5}{3}} & 1 \leq k \leq 5, \\ Ak^{-\frac{5}{3}} & k > 5, \end{cases} \tag{3.35}$$

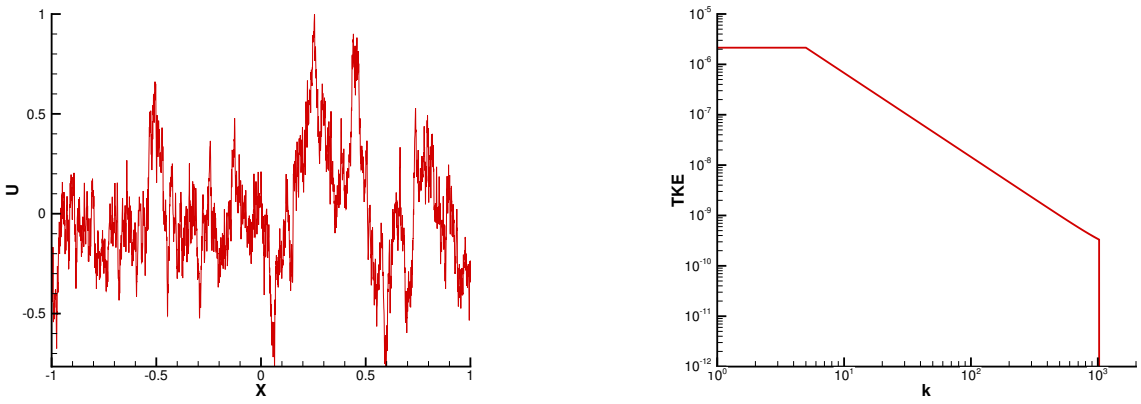

(a) (b)

Figure 3.3: Initial condition (left) and the initial energy spectrum (right)

where k is an integer varying from 1 to 1280. For each k, the velocity u has a random phase angle, β, in $[-\pi, \pi]$.

$$u(x) = \sum_{i}^{n} (2E_0(k_i))^{\frac{1}{2}} sin(k_i x + \beta_i) + 1 \tag{3.36}$$

A is a constant to make the turbulence intensity $\frac{u'}{\bar{u}} = 0.7\%$, where $u' = \sqrt{\frac{\sum_{i=1}^{N}(u_i - \bar{u})^2}{N}}$, $\bar{u} = 1$. The two boundaries are set to be periodic due to the periodicity of the initial condition.

3.1.5 Grid and Spatial filter

The computational domain is $[-1, 1]$. A mesh refinement study indicated that 8,192 cells with the 3^{rd} order FR/CPR method are required to resolve all the scales. Figure 3.4 shows the energy spectrum at for the linear wave propagation with the same initial condition. There is no visible decay at even the highest frequency. We consider the simulation at this resolution a DNS, and denote $\Delta x_{DNS} = \frac{2}{8192}$. In the a priori study, the DNS solution is filtered with a box filter with $\Delta = 32\Delta x_{DNS}$. The filtered solution is obtained

$$\hat{u}_{i,j} = \sum_{n=1}^{N} \sum_{m=1}^{K+1} u_{n,m} * w_{n,m,i,j}, \tag{3.37}$$

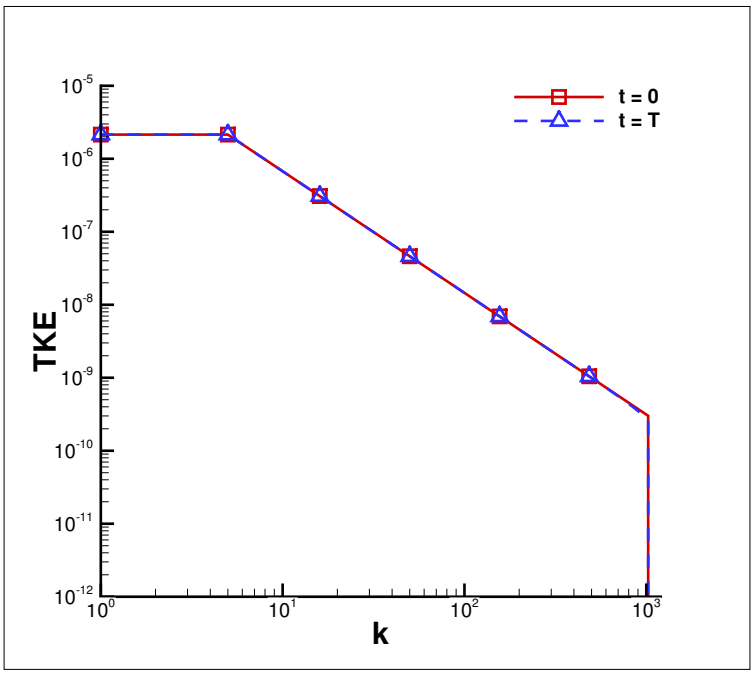

Figure 3.4: Turbulent energy spectrum at $t = 0$ and $t = T$

where N is the number of cells in the filtering stencil of the current degree of freedom and K is the degree of the polynomial of the solution. In each cell, a Gauss quadrature rule was implemented and w is the weighting coefficient. Then the filtered solution on the DNS grid is projected to the (coarse) LES grid if necessary to serve as the LES solution. In the current LES cell, the projected solution at each solution point j is calculated using

$$\int_{\Delta x_{LES}} L_k \sum_{j}^{K+1} L_j \hat{u}_{i,j} dx = \sum_{n=1}^{N} \int_{\Delta x_{DNS}} L_k \sum_{j}^{K+1} l_j \hat{u}_{n,j} dx, \tag{3.38}$$

where L_j is the shape function defined based on the solution points of the LES cell, l_j is the shape function based on the solution points of the DNS cell. In the a posteriori study, we do the same thing to the DNS initial condition to generate the LES initial condition.

In Figure 3.5, $\Delta = 8\Delta x_{DNS}$, $\Delta x_{LES} = 4\Delta x_{DNS}$ are used to demonstrate the filtering operation. Different cell sizes for LES were tested to evaluate the influence of the truncation error and the SGS modeling error. We call the filter used on the initial condition the first

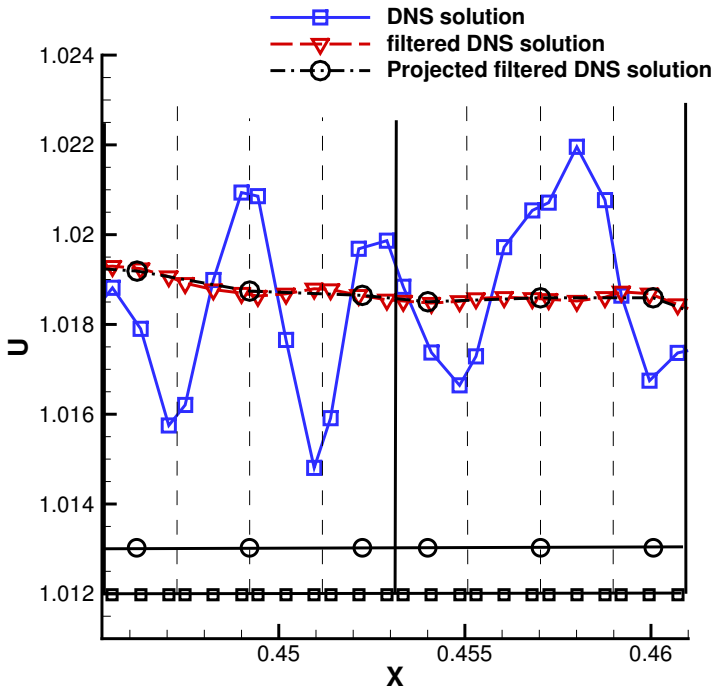

Figure 3.5: Comparison of various solutions(square: fine mesh solution points; circle: coarse mesh solution points)

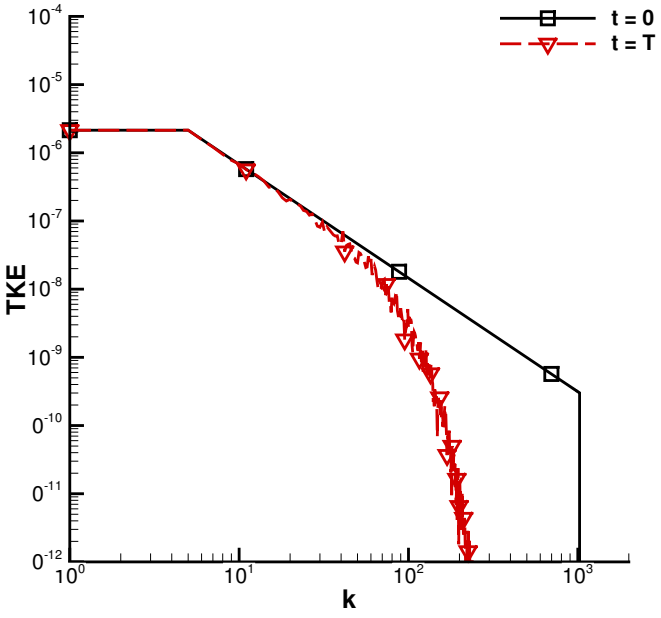

Figure 3.6: The energy spectrum at two different times

filter and the filter used in deciding the coefficient of the dynamic model or computing the resolved SGS stress the test filter. The test filter width is 2 times the width of the first filter, which makes $\gamma = 2$.

3.1.6 Numerical Results and Discussions

In this section, the results for the a priori and a posteriori tests are presented. Due to the nonlinear convection term, shock waves start to appear after a certain time. Thus all results are obtained at a time $T = 0.1$, when the solution is still smooth. Figure 3.1.6 shows the energy spectrum at $t = 0$ and $t = T$ of the DNS. We can see that the high frequencies are damped out by the physical viscosity while the lower frequencies remain.

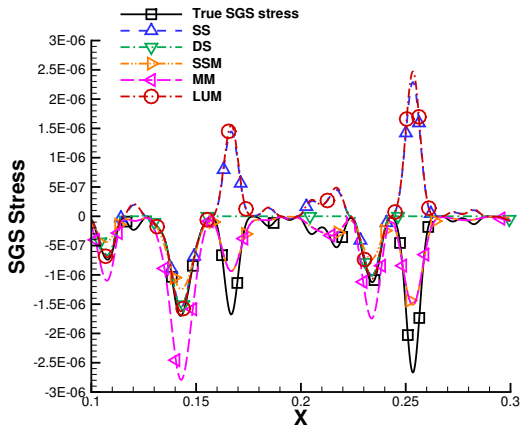

(a) $\frac{\Delta x_{LES}}{\Delta x_{DNS}} = 1$

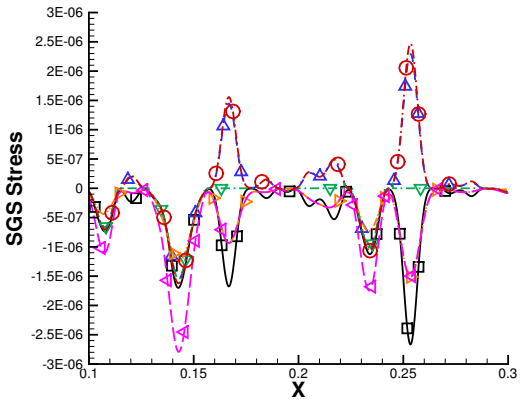

(b) $\frac{\Delta x_{LES}}{\Delta x_{DNS}} = 2$

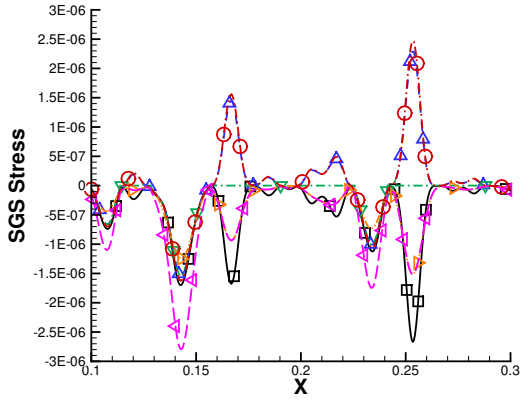

(c) $\frac{\Delta x_{LES}}{\Delta x_{DNS}} = 4$

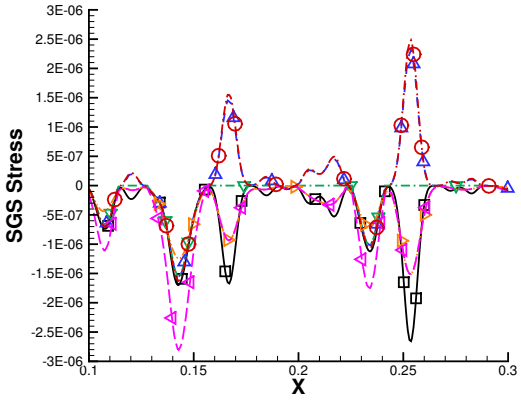

(d) $\frac{\Delta x_{LES}}{\Delta x_{DNS}} = 8$

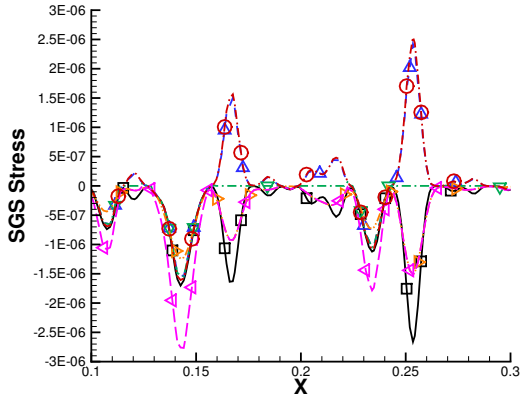

(e) $\frac{\Delta x_{LES}}{\Delta x_{DNS}} = 16$

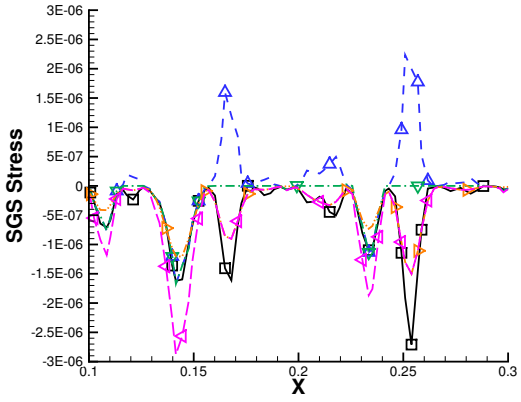

(f) $\frac{\Delta x_{LES}}{\Delta x_{DNS}} = 32$

Figure 3.7: The SGS stress comparison in the a priori tests

Table 3.1: Correlation coefficients of a priori test

$\frac{\Delta x_{LES}}{\Delta x_{DNS}}$	SS	DS	SSM	Mix	LUM
1	-0.10	0.6	0.95	0.89	-0.09
2	-0.10	0.6	0.95	0.89	-0.09
4	-0.10	0.6	0.95	0.89	-0.09
8	-0.10	0.6	0.95	0.89	-0.09
16	-0.10	0.6	0.95	0.89	-0.09
32	-0.09	0.59	0.95	0.88	0.04

3.1.6.1 A Priori Tests

Figure 3.7 shows the SGS stress computed using different models based on the filtered-DNS data at $t = T$ with various mesh resolutions and a fixed filter width of $\Delta = 32\Delta x_{DNS}$. The ratio between the cell size of LES and DNS is (a) 1, (b) 2, (c) 4, (d) 8, (e) 16, (f) 32. For the SS model, c_s is set to the default value of 0.2 for all of the comparisons. For ILES, the SGS stress is 0 everywhere. From Figure 3.7, we can make some general observation regardless of mesh resolutions:

- No models are able to predict the true stress in both amplitude and phase (peaks and valleys).
- Both the SSM and MM always correctly predict the phase of the true stress.
- SS correctly predicts the phase of the true stress about half the time, and DS agrees with the SS when the phase is correct. When the stress computed with SS has a wrong sign, DS sets the stress to 0.
- LUM agrees very well with SS in SGS prediction with enough grid resolution, but diverges for the coarsest mesh.

Obviously the good phase prediction capability of the MM is due to the dominant SSM term. Next we examine the correlation of the modeled stress with the true stress. Table 3.1 presents the correlation coefficients between the true SGS and the ones computed with the

Table 3.2: Correlation coefficients of a posteriori test

$\frac{\Delta x_{LES}}{\Delta x_{DNS}}$	SS	DS	SSM	Mix	LUM
1	-0.08	0.6	0.95	0.89	-0.06
2	-0.08	0.6	0.95	0.89	-0.07
4	-0.08	0.6	0.95	0.89	-0.07
8	-0.08	0.6	0.95	0.89	-0.07
16	-0.08	0.6	0.95	0.89	–
32	-0.10	0.57	0.92	0.85	–

models. Clearly the SSM and the MM models perform the best. The mesh resolution Δx_{LES} does not have any significant influence on the model behavior, except for LUM. To further evaluate the behavior of these models in an actual computation, we perform a posteriori tests next.

3.1.6.2 A Posteriori Tests

In this test, the filtered 1D Burgers' equation is solved with different models on different meshes with a fixed filter size $\Delta = 32\Delta x_{DNS}$. The results at the same physical time $t = T$ are compared. Figure 3.8 shows the SGS stress computed using different models with various mesh resolution.

In Figure 3.8, we can see that the results are very similar to those in the a priori test. We can draw the same conclusions here. Table 3.2 shows the correlation coefficients for all the a posteriori tests. The SGS stresses computed by SSM and the MM always show high correlations with the true SGS stress. The DS comes the second. The SS and the LUM models yield very low correlation with the true SGS stress. LUM diverged for some cases and the correlation is not available. The LES mesh resolution does not have a significant influence on the model behavior, except for LUM.

Figure 3.9 shows the comparison of the solution, $\hat{u}$, for $\frac{\Delta x_{LES}}{\Delta x_{DNS}}$. The solution computed with the true SGS stress is right on top of the filtered DNS solution. The solutions computed with models and ILES all show differences with the filtered DNS solution. Table 3.3 shows

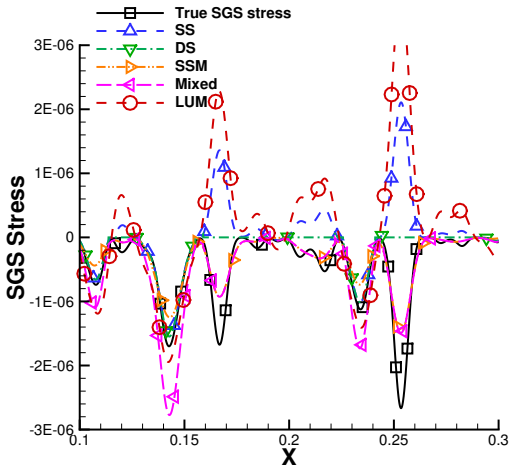

(a) $\frac{\Delta x_{LES}}{\Delta x_{DNS}} = 1$

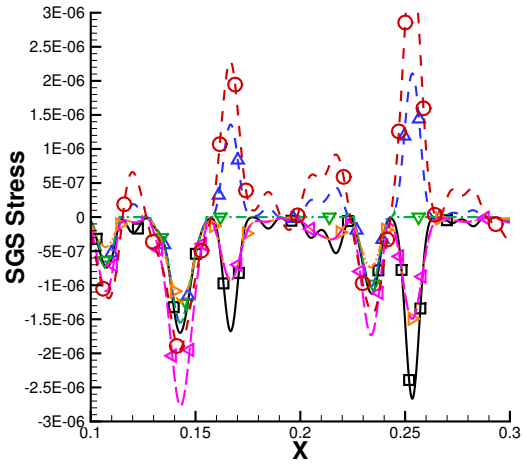

(b) $\frac{\Delta x_{LES}}{\Delta x_{DNS}} = 2$

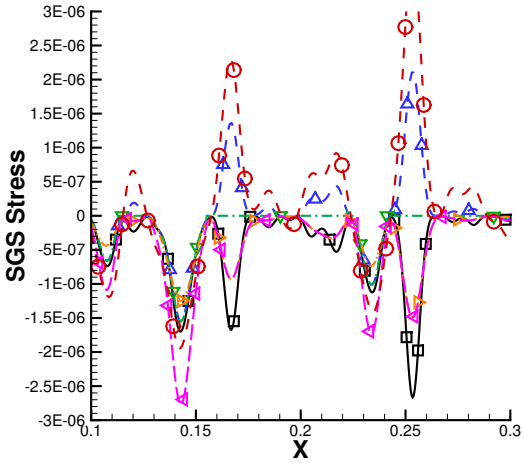

(c) $\frac{\Delta x_{LES}}{\Delta x_{DNS}} = 4$

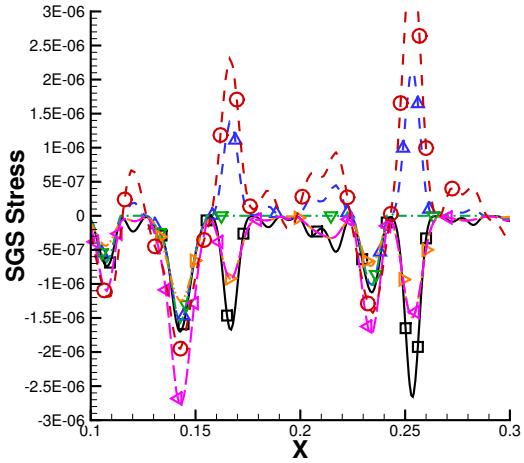

(d) $\frac{\Delta x_{LES}}{\Delta x_{DNS}} = 8$

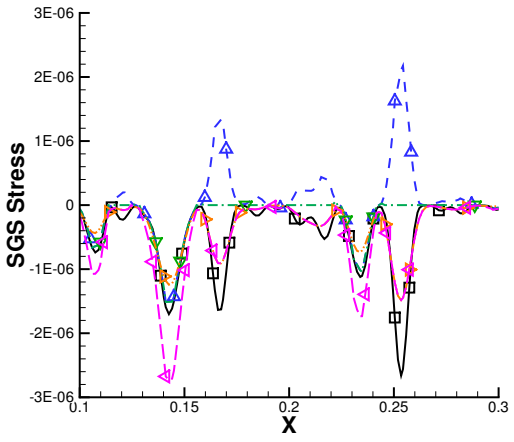

(e) $\frac{\Delta x_{LES}}{\Delta x_{DNS}} = 16$

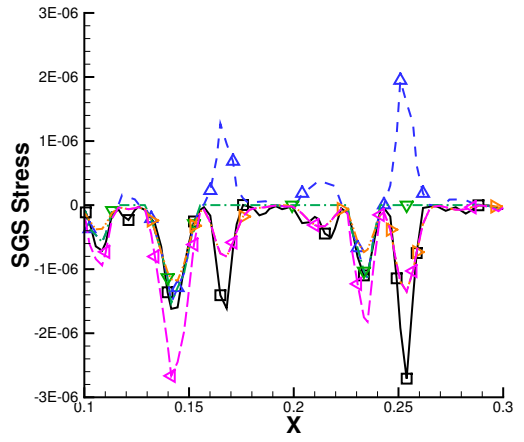

(f) $\frac{\Delta x_{LES}}{\Delta x_{DNS}} = 32$

Figure 3.8: The SGS stress comparison in the a posteriori tests

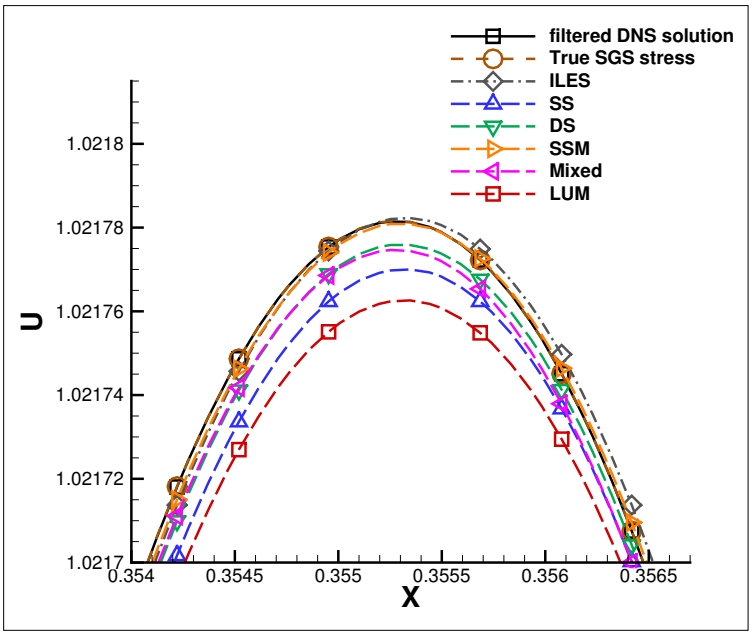

Figure 3.9: Solution Comparison

Table 3.3: L2 norm error of the solution

$\frac{\Delta x_{LES}}{\Delta x_{DNS}}$	True stress	ILES	SS	DS	SSM	Mix	LUM
1	2.03E-08	1.14E-05	1.57E-05	8.88E-06	7.02E-06	6.19E-06	1.80E-05
2	2.13E-08	1.14E-05	1.57E-05	8.88E-06	7.02E-06	6.18E-06	3.02E-05
4	4.60E-08	1.14E-05	1.57E-05	8.88E-06	7.01E-06	6.17E-06	5.62E-05
8	4.91E-07	1.14E-05	1.57E-05	8.97E-06	6.94E-06	6.25E-06	1.07E-04
16	1.09E-05	1.46E-05	2.01E-05	1.49E-05	1.18E-05	1.35E-05	–
32	1.38E-04	1.38E-04	1.41E-04	1.39E-04	1.37E-04	1.39E-04	–

the L2 norm error comparison. When the LES mesh is sufficiently fine, it is clear that the SSM and the MM produced the best solutions. This is because both models show the best correlation with the true SGS stress. When the LES mesh is coarse, the truncation error is dominant. The results with any model and with the true SGS stress are comparable. Clearly ILES is the best choice because it costs the least.

3.1.6.3 Sensitivity of the Models to the Mesh Resolution

Given the fixed filter width, we compare models' behavior on different mesh resolution. Figure 3.10 shows different modeled SGS comparison with respect to different. The $ratio = \frac{\Delta x_{LES}}{\Delta x_{DNS}}$. We can see that both in the a priori and the a posteriori tests, all the models shows no sensitivity to Δx_{LES} except for the LUM.

3.1.6.4 Effects of Truncation Error vs. SGS Model Error

In large eddy simulations, the numerical results depend on many factors, including the flow condition, the initial and boundary conditions, the numerical method, the computational mesh, the filter and the SGS model. Some of the factors are physical and others are numerical, and they intertwine together to produce the final solution. At the most fundamental level, the filter width Δ in a LES is perhaps the most critical parameter, and Pope discussed the importance of the filter width in [41]. The true LES solution can be obtained by filtering the DNS solution using this Δ. In reality, however, the filter width is often implicitly tied with the mesh size. In such cases, mesh refinement convergence studies become impossible to perform because the filter size is always a variable. One can only see convergence when the mesh size approaches that required of a DNS simulation.

Generally speaking, we want to accurately predict the SGS stress using the numerical solution at the "resolved scale". The filtered solution $\hat{u}$ is always taken to be the solution at the "resolved scale". Let's consider the box filter here. When a solution is filtered with a width Δ , we often state that waves with shorter wavelengths than Δ are filtered out.

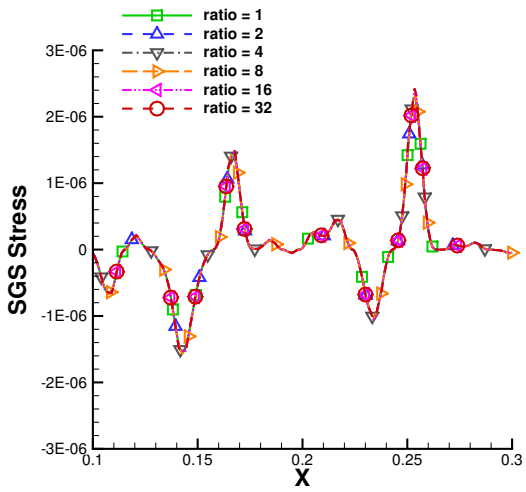

(a) SGS modeled by SS, a priori

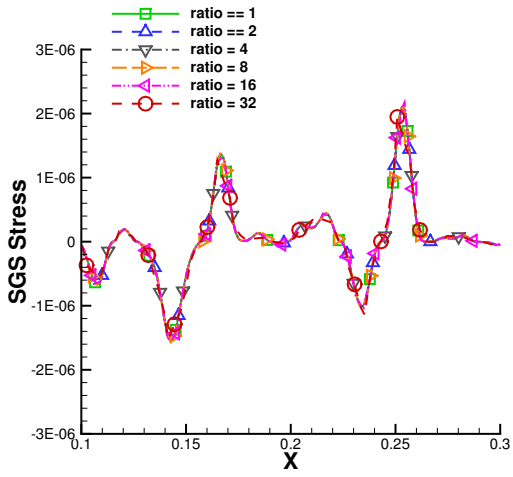

(b) SGS modeled by SS, a posteriori

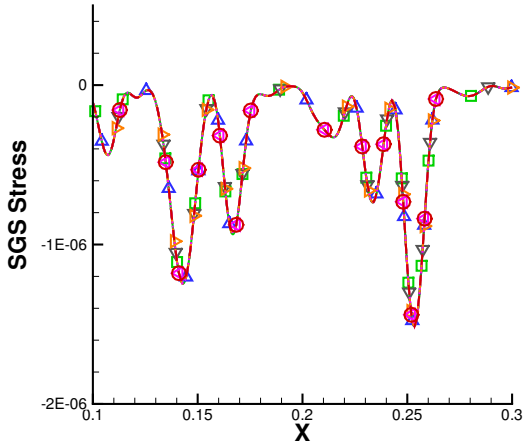

(c) SGS modeled by SSM, a priori

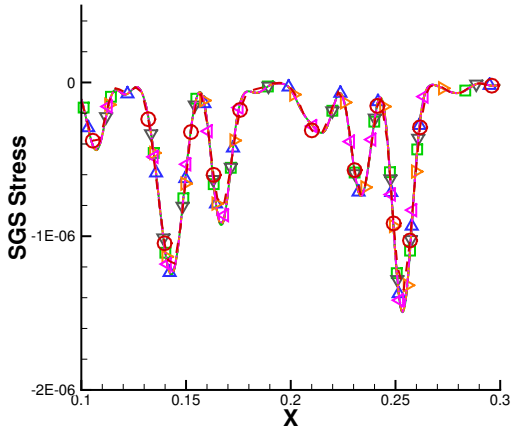

(d) SGS modeled by SSM, a posteriori

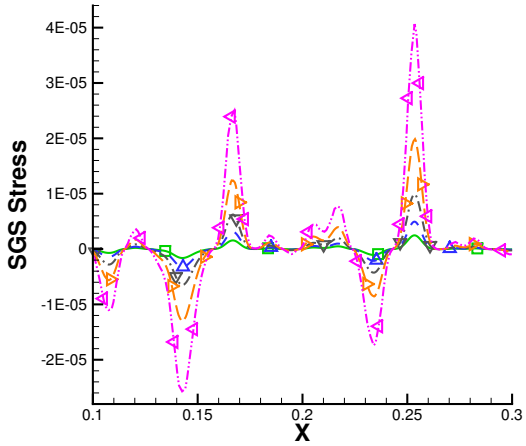

(e) SGS modeled by LUM, a priori

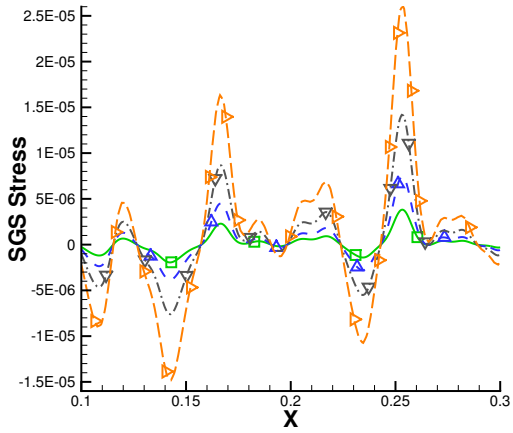

(f) SGS modeled by LUM, a posteriori

Figure 3.10: The modeled SGS with different mesh resolution

In fact, waves of wavelengths of 2Δ and 4Δ are heavily damped out too. Based on our analysis, we can see that the amplitudes of 2Δ and 4Δ waves are reduced by 36% and 10% respectively [47]. If we accept 36% filtering error as acceptable, the "resolved scale" should be 2Δ instead of Δ. In addition, numerical methods also have limited resolution depending on the "points per wave" (PPW) or "degrees of freedom per wave" (DOFPW). Let's assume that for the present 3rd order FR/CPR scheme, 9 DOFPW is required to resolve a wave. In other words, 3 elements are needed for a wave since there are 3 DOFs in one element. A truly resolved scale must meet the accuracy requirement from both the filtering operator and the numerical scheme. In this particular case, the resolved scale is

$$S_R = max(3\Delta x_{LES}, 2\Delta), \tag{3.39}$$

In order to have the resolved scale determined by the given filter width, Δx_{LES} should satisfy the following requirement

$$\Delta x_{LES} \leq \frac{2\Delta}{3} \tag{3.40}$$

In the case of second-order finite volume methods, each element has 1 solution unknown. If one requires 20 PPW for accuracy, the resolved scale is then

$$S_R = max(20\Delta x_{LES}, 2\Delta). \tag{3.41}$$

If one chooses Δx_{LES} as the filter width, the resolved scale is 20 times larger than the filter width because of the accuracy requirement. In other words, the numerical truncation error is dominant in the LES results. This is the reason why we see smaller and smaller differences between the ILES and LES with SGS models with the Δx_{LES} increase.

3.2 Investigation of Scale Similarity

Since the pioneering work by Bardina et al on the SSM [9] for incompressible flow, there has been an extensive effort in evaluating its performance by comparing with other SGS models [60] [40]. Furthermore the SSM has been extended to other flow problems including compressible flow [61] and combustion [62]. Direct numerical simulations and experimental measurements [45] [16] [63] have demonstrated scale similarity in turbulent flows. Many a priori tests using experimental or DNS data have shown a high correlation between the true stress and the modeled SGS based on the SSM [45], which agree with our observation in last section. In Bardina's original SSM, the second filter or test filter has the same width as the first one. It was proven by Speziale [64] that the Bardina constant must be 1 to satisfy Galilean invariance. The present analysis to be shown later confirms this result. Other researchers suggested using a different filter width for the second filter, e.g., in [45], and many approaches were suggested to determine the Bardina constant [65] [63]. In the present study, we found that the SSM modeled stress is almost right on top of the true SGS stress when the constant 4, i.e,

$$\frac{L}{\tau_{true}} = 4. \tag{3.42}$$

When we first saw the relation (3.42), we suspected that this was a bug. After we tested different initial conditions, we were convinced that it was not a bug. The fact that relation (3.42) is true for arbitrarily-generated random initial conditions prompted us to look for a deeper reason resulting in the following analysis.

3.2.1 Analysis of Scale Similarity with a Single Fourier Mode

For the sake of simplicity without loss of generality, we consider periodic data $u(x)$ at a given time on domain $[-\pi, \pi]$. The solution can be decomposed into the following Fourier modes

$$u(x) = \sum_{n=0}^{inf} a_n e^{inx}, \tag{3.43}$$

where $i = \sqrt{-1}$, and n is the wave number. To illustrate the basic idea, we first consider a single Fourier mode, i.e., $u(x) = e^{inx}$ and the top hat filter. The filtered solution is then

$$\hat{u}(x) = \frac{1}{\Delta}\int_{x-\frac{\Delta}{2}}^{x+\frac{\Delta}{2}} e^{in\xi}d\xi = sinc(\frac{n\Delta}{2})\cdot e^{inx}, \tag{3.44}$$

where $sinc(\frac{n\Delta}{2}) = \frac{sin\frac{n\Delta}{2}}{\frac{n\Delta}{2}}$. Obviously the filter only changes the magnitude of the solution, but not the phase. In addition, we have

$$\hat{u\hat{u}}(x) = \frac{1}{\Delta}\int_{x-\frac{\Delta}{2}}^{x+\frac{\Delta}{2}} e^{i2n\xi}d\xi = sinc(n\Delta)\cdot e^{i2nx}. \tag{3.45}$$

The SGS stress is then

$$\tau = \hat{u\hat{u}} - \hat{u}\hat{u} = sinc(n\Delta)\cdot e^{i2nx} - sinc^2(\frac{n\Delta}{2})\cdot e^{i2nx} = [sinc(n\Delta) - sinc^2(\frac{n\Delta}{2})]e^{i2nx}. \tag{3.46}$$

Next we apply a second filter with a width of $\Delta_2 = \gamma\Delta$ to the resolved variable to obtain

$$\tilde{\hat{u}}(x) = \frac{1}{\gamma\Delta}\int_{x-\frac{\gamma\Delta}{2}}^{x+\frac{\gamma\Delta}{2}} \hat{u}(\xi)d\xi = sinc(\frac{n\Delta}{2})sinc(\frac{\gamma n\Delta}{2})e^{inx}, \tag{3.47}$$

and

$$\tilde{\hat{u}\hat{u}}(x) = \frac{1}{\gamma\Delta}\int_{x-\frac{\gamma\Delta}{2}}^{x+\frac{\gamma\Delta}{2}} \hat{u}(\xi)\hat{u}(\xi)d\xi = sinc^2(\frac{n\Delta}{2})sinc(\frac{\gamma n\Delta}{2})e^{i2nx}. \tag{3.48}$$

The SGS stress of the resolved scale is then

$$L = \tilde{\hat{u}\hat{u}} - \tilde{\hat{u}}\tilde{\hat{u}} = sinc^2(\frac{n\Delta}{2})(sinc(\gamma n\Delta) - sinc^2(\frac{\gamma n\Delta}{2}))e^{i2nx}. \tag{3.49}$$

From (3.46) and (3.49), we obtain

$$\frac{L}{\tau} = \frac{sinc^2(\frac{n\Delta}{2})(sinc(\gamma n\Delta) - sinc^2(\frac{\gamma n\Delta}{2}))}{sinc(n\Delta) - sinc^2(\frac{n\Delta}{2})}. \tag{3.50}$$

In the limit of small $n\Delta$, we have

$$sinc(n\Delta) = 1 - \frac{(n\Delta)^2}{6} + O(n\Delta)^4. \tag{3.51}$$

Therefore, we obtain

$$\frac{L}{\tau} = \frac{[1 - \frac{(n\Delta)^2}{12} + O(n\Delta)^4][-\frac{(\gamma n\Delta)^2}{6} + \frac{(\gamma n\Delta)^2}{12} + O(n\Delta)^4]}{-\frac{(n\Delta)^2}{6} + \frac{(n\Delta)^2}{12} + O(n\Delta)^4} = \gamma^2 + O(n\Delta)^2. \tag{3.52}$$

Note that the error term is quadratic. In the special case of $\gamma = 2$, $L = 4\tau$. As it turns out this result is also true for the Gaussian filter. The filtered solution with a Gaussian filter is

$$\hat{u}(x) = \int_{-\inf}^{\inf} \sqrt{(\frac{6}{\pi\Delta^2})} e^{-\frac{6(x-\xi)^2}{\Delta^2}} ein\xi d\xi = sqrt(\frac{6}{\pi\Delta^2}) \int_{-\inf}^{\inf} e^{-\frac{6(x-\xi)^2}{\Delta^2}} ein\xi d\xi. \tag{3.53}$$

Set $X = \frac{\sqrt{6}(x-\xi)}{\Delta}$, so that $\xi = x - \frac{\Delta}{\sqrt{6}}X$, $d\xi = -\frac{\Delta}{\sqrt{6}}dX$. Thus, we have

$$\hat{u}(x) = \sqrt{\frac{6}{\pi\Delta^2}} \cdot \frac{\Delta}{\sqrt{6}} \int_{-\inf}^{\inf} e^{-X^2 + in(x - \frac{\Delta}{\sqrt{6}}X)} dX = \sqrt{\frac{1}{pi}} e^{inx} \int_{-inf}^{inf} e^{-X^2 - in\frac{\Delta}{\sqrt{6}}X} dX = e^{inx} e^{-\frac{(n\Delta)^2}{24}}. \tag{3.54}$$

Similarly we can derive the following result

$$\hat{uu}(x) = \int_{-inf}^{inf} \sqrt{\frac{6}{\pi\Delta^2}} e^{-\frac{6(x-\xi)^2}{\Delta^2}} e^{i2nx} d\xi = \sqrt{\frac{1}{pi}} e^{i2nx} \int_{-inf}^{inf} e^{-X^2 - i2n\frac{\Delta}{\sqrt{6}}X} dX = e^{i2nx} e^{-\frac{(n\Delta)^2}{6}}. \tag{3.55}$$

The SGS stress is them

$$\tau = \hat{uu} - \hat{u}\hat{u} = e^{i2nx} e^{-\frac{(n\Delta)^2}{6}} - e^{i2nx} e^{-\frac{(n\Delta)^2}{12}} = e^{i2nx} e^{-\frac{(n\Delta)^2}{6}} [1 - e^{-\frac{(n\Delta)^2}{12}}]. \tag{3.56}$$

Again we apply a second filter with a width of $\Delta_2 = \gamma\Delta$ to the resolved field to obtain

$$\tilde{\hat{u}}(x) = e^{-\frac{(n\Delta)^2}{24}} \tilde{u}(x) = e^{-\frac{(n\Delta)^2}{24}} e^{-\frac{(\gamma n\Delta)^2}{24}} e^{inx}. \tag{3.57}$$

and

$$\tilde{\hat{u}\hat{u}}(x) = e^{-\frac{(n\Delta)^2}{12}} \tilde{uu}(x) = e^{-\frac{(n\Delta)^2}{12}} e^{-\frac{(\gamma n\Delta)^2}{6}} e^{i2nx}. \tag{3.58}$$

The SGS stress of the resolved scale is

$$L = \tilde{\hat{u}\hat{u}} - \tilde{\hat{u}}\tilde{\hat{u}} = e^{i2nx} e^{-\frac{(1+2\gamma^2)(n\Delta)^2}{12}} [1 - e^{\frac{(\gamma n\Delta)^2}{12}}]. \tag{3.59}$$

From /eqnrefe:sgs gauss and /eqnrefe:L gauss, we obtain

$$\frac{L}{\tau} = e^{\frac{(1-2\gamma^2)(n\Delta)^2}{12}} \frac{1 - e^{\frac{(\gamma n\Delta)^2}{12}}}{1 - e^{\frac{(n\Delta)^2}{12}}}. \tag{3.60}$$

In the limit of small $n\Delta$, we have

$$\frac{L}{\tau} = (1 + O(n\Delta)^2) \frac{1 - 1 - \frac{(\gamma n\Delta)^2}{12} + O(n\Delta)^4}{1 - 1 - \frac{(n\Delta)^2}{12} + O(n\Delta)^4} = \gamma^2 + O(n\Delta)^2. \tag{3.61}$$

3.2.2 Analysis of Scale Similarity with All Fourier Modes

Next we consider a solution with all the Fourier modes, i.e.,

$$u(x) = \sum_{n=0}^{inf} a_n e^{inx}. \tag{3.62}$$

With the top hat filter, we obtain the following filtered solution

$$\hat{u}(x) = \sum_{n=0}^{inf} a_n sinc(\frac{n\Delta}{2}) \cdot e^{inx}. \tag{3.63}$$

In addition, we have

$$\hat{uu}(x) = \sum_{n=0}^{inf} \sum_{m=0}^{inf} a_n a_m sinc \frac{(n+m)\Delta}{2} e^{i(n+m)x}. \tag{3.64}$$

The SGS stress is then

$$\tau = \hat{uu} - \hat{u}\hat{u} = \sum_{n=0}^{inf}\sum_{m=0}^{inf} a_n a_m [sinc\frac{(n+m)\Delta}{2} - sinc(\frac{n\Delta}{2})sinc(\frac{m\Delta}{2})]e^{i(n+m)x}. \tag{3.65}$$

Next we apply a second filter with a width of $\gamma\Delta$ to the resolved variable

$$\tilde{\hat{u}} = \sum_{n=0}^{inf} a_n sinc(\frac{n\Delta}{2})sinc(\frac{\gamma n\Delta}{2})e^{inx}, \tag{3.66}$$

and

$$\tilde{\hat{u}}\tilde{\hat{u}}\hat{u} = \sum_{n=0}^{inf}\sum_{m=0}^{inf} a_n a_m sinc(\frac{n\Delta}{2})sinc(\frac{m\Delta}{2})sinc(\frac{\gamma(n+m)\Delta}{2})e^{i(n+m)x}. \tag{3.67}$$

The SGS stress of the resolved scale is then

$$L = \tilde{\hat{u}}\tilde{\hat{u}}\hat{u} - \tilde{\hat{u}}\tilde{\hat{u}} = \sum_{n=0}^{inf}\sum_{m=0}^{inf} a_n a_m sinc(\frac{n\Delta}{2})sinc(\frac{m\Delta}{2})(sinc(\frac{\gamma(n+m)\Delta}{2}) - sinc(\frac{\gamma n\Delta}{2})sinc(\frac{\gamma m\Delta}{2}))e^{i(n+m)x}. \tag{3.68}$$

Now let's consider each term in /eqnrefe:sgs all and /eqnrefe:L all. It is obvious that

$$\frac{L_{nm}}{\tau_{nm}} = \frac{sinc(\frac{n\Delta}{2})sinc(\frac{m\Delta}{2})(sinc(\frac{\gamma(n+m)\Delta}{2}) - sinc(\frac{\gamma n\Delta}{2})sinc(\frac{\gamma m\Delta}{2}))}{sinc\frac{(n+m)\Delta}{2} - sinc(\frac{n\Delta}{2})sinc(\frac{m\Delta}{2})} = \gamma^2 + O[(n+m)\Delta]^2. \tag{3.69}$$

Therefore, we have

$$\frac{L}{\tau} = \gamma^2 + O[(n+m)\Delta]^2. \tag{3.70}$$

n the same limit. The analysis with the Gaussian filter is similar and is not repeated here.

3.2.3 Analysis of Scale Similarity in 2D

In two dimensions, we only perform a single mode analysis with the top hat filter. Consider the following two dimensional velocity field

$$u(x,y) = e^{inx}e^{imy}, v(x,y) = e^{ipx}e^{iqy}. \tag{3.71}$$

The filtered solution is then

$$\hat{u}(x,y) = \frac{1}{\Delta^2}\int_{x-\frac{\Delta}{2}}^{x+\frac{\Delta}{2}}\int_{y-\frac{\Delta}{2}}^{y+\frac{\Delta}{2}} e^{in\xi}e^{im\eta}d\eta d\xi = e^{inx}e^{imy}\cdot sinc(\frac{n\Delta}{2})sinc(\frac{m\Delta}{2}), \tag{3.72}$$

$$\hat{v}(x,y) = \frac{1}{\Delta^2}\int_{x-\frac{\Delta}{2}}^{x+\frac{\Delta}{2}}\int_{y-\frac{\Delta}{2}}^{y+\frac{\Delta}{2}} e^{ip\xi}e^{iq\eta}d\eta d\xi = e^{ipx}e^{iqy}\cdot sinc(\frac{p\Delta}{2})sinc(\frac{q\Delta}{2}). \tag{3.73}$$

In addition, we have

$$\hat{uv}(x,y) = \frac{1}{\Delta^2}\int_{x-\frac{\Delta}{2}}^{x+\frac{\Delta}{2}}\int_{y-\frac{\Delta}{2}}^{y+\frac{\Delta}{2}} e^{i(n+p)\xi}e^{i(m+q)\eta}d\eta d\xi = e^{i(n+p)x}e^{i(m+q)y}\cdot sinc(\frac{(n+p)\Delta}{2})sinc(\frac{(m+q)\Delta}{2}). \tag{3.74}$$

The SGS stress is then

$$\begin{aligned}\tau &= \hat{uv} - \hat{u}\hat{v}\\ &= e^{i(n+p)x}e^{i(m+q)y}[sinc(\frac{(n+p)\Delta}{2})sinc(\frac{(m+q)\Delta}{2})\\ &- sinc(\frac{n\Delta}{2})sinc(\frac{m\Delta}{2})sinc(\frac{p\Delta}{2})sinc(\frac{q\Delta}{2})].\end{aligned} \tag{3.75}$$

Applying a second filter with a width $\gamma\Delta$ to the resolved variable, we obtain

$$\tilde{\hat{u}} = e^{inx}e^{imy}\cdot sinc(\frac{n\Delta}{2})sinc(\frac{m\Delta}{2})sinc(\frac{\gamma n\Delta}{2})sinc(\frac{\gamma m\Delta}{2}), \tag{3.76}$$

and

$$\tilde{\hat{v}} = e^{ipx}e^{iqy}\cdot sinc(\frac{p\Delta}{2})sinc(\frac{q\Delta}{2})sinc(\frac{\gamma p\Delta}{2})sinc(\frac{\gamma q\Delta}{2}), \tag{3.77}$$

Denote $\alpha = sinc(\frac{n\Delta}{2})sinc(\frac{m\Delta}{2})sinc(\frac{p\Delta}{2})sinc(\frac{q\Delta}{2})$. Then we have

$$\tilde{\hat{u}}\tilde{\hat{v}} = \alpha\tilde{uv}, \tilde{\hat{u}}\tilde{\hat{v}} = \alpha\tilde{u}\tilde{v}. \tag{3.78}$$

The SGS stress of the resolved scale is then

$$\begin{aligned} L &= \hat{\tilde{u}}\hat{\tilde{v}} - \hat{\tilde{u}}\hat{\tilde{v}} = \alpha(\tilde{uv} - \tilde{u}\tilde{v}) \\ &= \alpha e^{i(n+p)x} e^{i(m+q)y} [sinc(\frac{\gamma(n+p)\Delta}{2}) sinc(\frac{\gamma(m+q)\Delta}{2}) \\ &- sinc(\frac{\gamma n\Delta}{2}) sinc(\frac{\gamma m\Delta}{2}) sinc(\frac{\gamma p\Delta}{2}) sinc(\frac{\gamma q\Delta}{2})]. \end{aligned} \tag{3.79}$$

From /eqnrefe:sgs 2d and /eqnrefe:L 2d, we obtain

$$\frac{L}{\tau} = \alpha \frac{sinc(\frac{\gamma(n+p)\Delta}{2}) sinc(\frac{\gamma(m+q)\Delta}{2}) - sinc(\frac{\gamma n\Delta}{2}) sinc(\frac{\gamma m\Delta}{2}) sinc(\frac{\gamma p\Delta}{2}) sinc(\frac{\gamma q\Delta}{2})}{sinc(\frac{(n+p)\Delta}{2}) sinc(\frac{(m+q)\Delta}{2}) - sinc(\frac{n\Delta}{2}) sinc(\frac{m\Delta}{2}) sinc(\frac{p\Delta}{2}) sinc(\frac{q\Delta}{2})}. \tag{3.80}$$

In the limit of small $(n+m+p+q)\Delta$, we have $\alpha \approx 1$, and

$$sinc(A+B) \cdot sinc(C+D) - sincA \cdot sincB \cdot sincC \cdot sincD = -\frac{AB+CD}{3} + HOT. \tag{3.81}$$

Finally, we derive the following result using /eqnrefe:ABCD

$$\frac{L}{\tau} \approx \gamma^2. \tag{3.82}$$

3.2.4 Implications for Large Eddy Simulation

The present analysis shows that perfect scale similarity exists for arbitrary (periodic) data including turbulence under the assumption that the spectrum contains relatively low frequency contents with respect to the filter width, regardless of amplitude and phase angle of each mode. Obviously for an arbitrary spectrum including both high and low frequency contents, the present analysis is not valid. This is easily seen in Figure 3.11, which displays the modeled and true SGS stress based on the full spectrum shown in Figure 3.3, using the same filter width which is $16\Delta_{DNS}$. The correlation between the modeled and true stresses is quite low.

Next let's examine whether /eqnrefe:l/tau 2d final is true in an actual LES. The promise

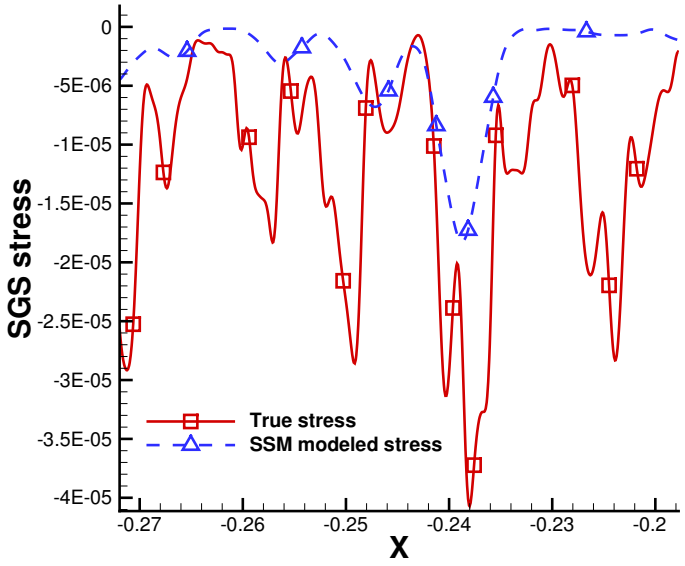

Figure 3.11: The true stress and the modeled stress for the full spectrum

of the SSM is that the SGS stress is highly correlated with the stress computed based on the resolved scale, taken to be $\hat{u}$. Take the top hat filter for example. Modes of smaller wavelength than D corresponding to the cutoff wavenumber k_Δ are filtered out. In LES, it is believed that the SGS stress from higher modes close to the cutoff wave number k_Δ plays an important role. In the next test, we therefore include modes between k_Δ and $2k_\Delta$ using a filter width D/2 to filter the spectrum shown in Figure 3.3. The filtered solution is then treated as DNS data, which is used to obtain the true stress. This true stress is also compared with the stresses computed using the SSM based on the resolved scale, i.e., $\hat{u}$. Two test filter widths are used corresponding to $\gamma = 1$ and 2. The results are displayed in Figure 3.11. Note that there is a reasonably high level of correlation between the stresses. The ratio between the true and modeled stresses are computed using simple averages

$$\frac{L}{\tau} = \frac{\langle L \rangle}{\langle \tau \rangle}. \tag{3.83}$$

The correlation coefficients and the average stress ratios from 10 realizations are summarized

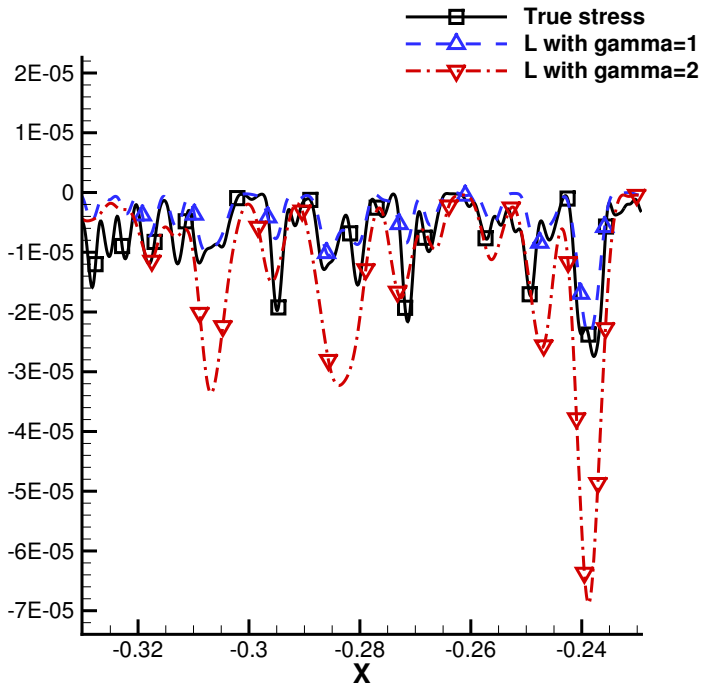

Figure 3.12: Comparison between the true stress computed with the SGS between k_Δ and $2k_\Delta$ and the modeled stresses computed using $\hat{u}$

in Table 3.1. The table confirms that the true stress shows a quite high correlation with the modeled stress, with an average correlation coefficients of 0.88 and 0.69 for $\gamma = 1$ and 2, respectively. In addition, $\gamma = 1$ demonstrates consistently higher correlation coefficients than $\gamma = 1$. This may indicate that one should use the same filter width for the second filter in an SSM implementation. Furthermore, the ratio of the averaged stresses remains a constant with different realizations, indicating that this ratio is only dependent on the spectrum. However, the ratio is much smaller than γ^2. This result appears to agree well with others in the literature [66] [45].

3.2.5 Investigation of Stability of Scale Similarity Model

In Bardina's original paper, the SSM was found unstable in some simulations when used with a central finite difference scheme. To remedy the instability, a MM with the DS model was developed to stabilize the simulations. In this section, we attempt to show that the extra dissipation added by the MM is not necessary for the FR/CPR method which has embedded numerical dissipation to automatically damp high frequency modes. We first demonstrate that there is indeed a pile-up of high frequency modes with a central difference scheme in solving nonlinear equations such as the Burgers' equation, while there is no such pile-up with a dissipative high-order FR/CPR scheme. For this purpose, we conduct a numerical study with the initial condition of a single Fourier mode,

$$u(x) = 2(E_0(1))^{1/2} sin(\pi x) + 1. \tag{3.84}$$

where $= 2(E_0(1))^{1/2} = 0.012$. The 1D inviscid Burgers' equation is employed to mimic very high Reynolds number problems. We run the simulation until $t = 26$ when it is right before a shock wave develops. First, the upwind flux and the central flux are employed in the 3rd order FR/CPR scheme to compare their behaviors. Figure 3.2.5 shows the energy spectrum at $t = 26$ with different mesh resolutions. On the finest mesh, both the central and upwind

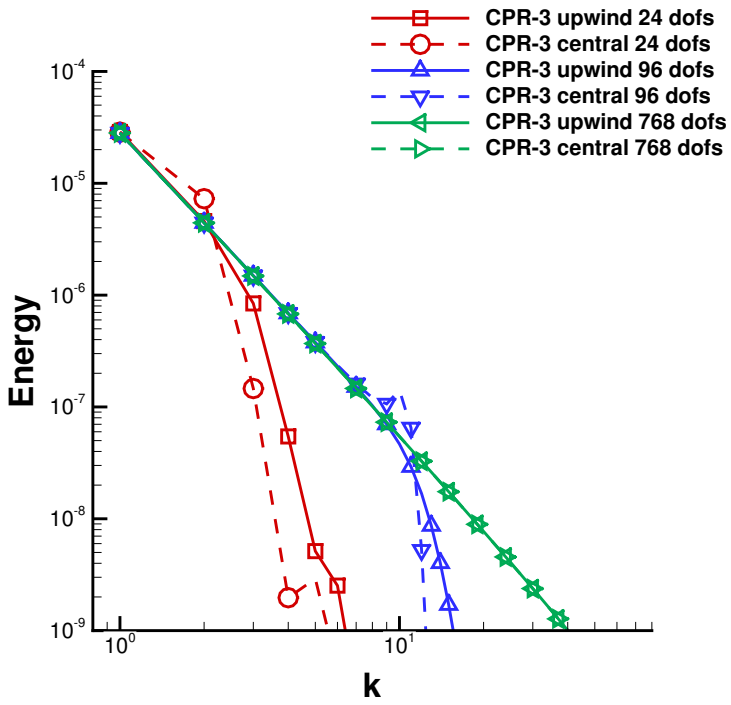

Figure 3.13: The spectrum of the upwind flux and the central flux with 3^{rd} order FR/CPR scheme at $t = 26$

schemes produced a converged solution within the visible energy spectrum in the figure. On the two coarser meshes, we can see clearly that energy is piling up at high frequencies on those meshes for the simulation with the central flux. But the upwind flux is able to smoothly damp out the high frequency modes so that they are never accumulated to cause stability problems. Next we test the influence of the SGS models on the energy spectrum. Figure 3.2.5 shows the spectrum comparison of the simulations with and without the SSM and MM. The filter width equals to the cell size. We can see that with the central flux, the SSM neither damps out all the energy accumulated at high frequencies nor accumulates more energy there. Thus the extra dissipation, i.e. the DS, is necessary to stabilize the simulation. It is worth noting that the extra dissipation, in the MM, also damps out the energy at some lower frequencies, which does harm to the resolved large scales. We also verify that a central difference finite difference scheme behaves similarly with the CPR scheme with a central flux. Figure 3.2.5 indeed shows that the 4th order central finite difference method has a similar

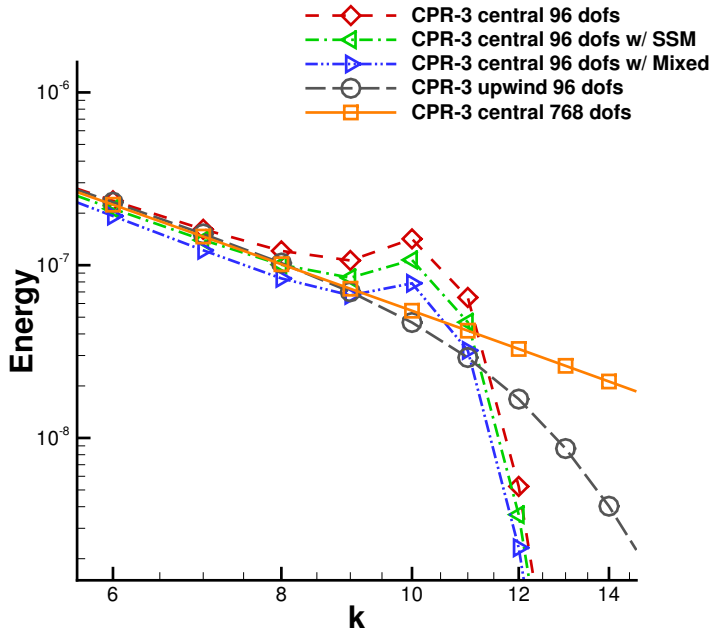

Figure 3.14: The spectrum of different models with 3^{rd} order FR/CPR scheme at $t = 26$

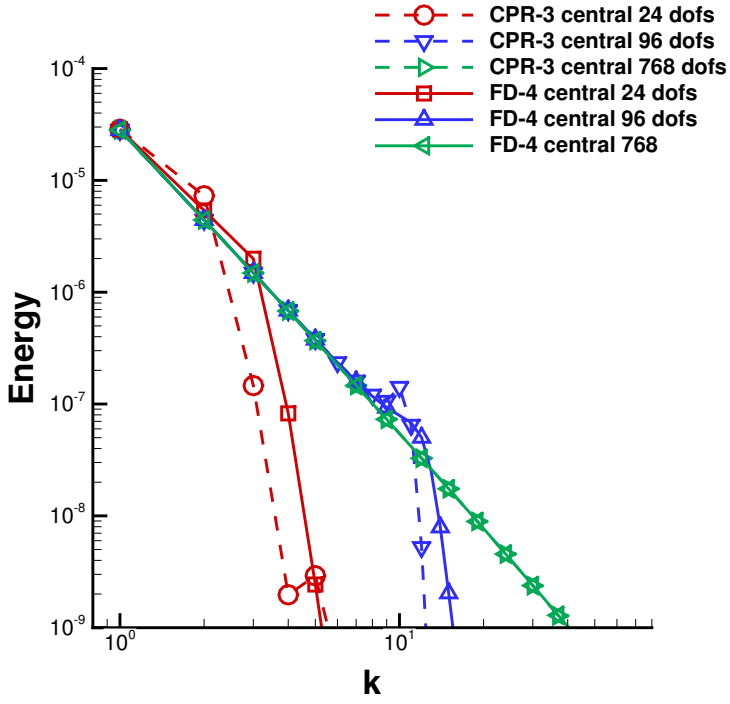

Figure 3.15: The spectrum of the 3^{rd} order FR/CPR scheme and the 4^{th} order finite difference scheme with the central flux at $t = 26$

performance to the 3rd order FR/CPR scheme with the central flux. This means that for schemes that are not dissipative, more dissipation may be necessary to stabilize the turbulent flow simulations with the SSM model. But for the dissipative ones, such as the FR/CPR method with an upwind flux, no extra dissipation is needed.

Chapter 4

Shock Capturing Techniques, the Flux Limiter, for the CPR Method

High-order numerical methods have shown their ability to produce accurate solutions with relatively small computational cost. In the previous chapters we presented the study of the high-order FR/CPR methds' behavior in aero-acoustics large eddy simulation. Its high-order accuracy and dissipation make it a very advantageous in solving these wide spectrum problems. However, for transonic or supersonic flow, the usage is limited. An outstanding issue with this method is how to deal with discontinuities, such as shocks in the flow, by removing the pseudo oscillations, while preserving the high order accuracy and good convergence.

One example of high-order scheme handling discontinuities is the essentially non-oscillatory scheme(ENO) [67] [68]. It selects a smooth flux stencil at each iteration. But due to its non-differentiability of the process, it's not possible to have a converged solution for steady problems. The weighted ENO(WENO) [69] [70] schemes can improve the behavior of convergence for steady problems, but still not satisfactory. The computational cost for each iteration is also much higher. Due to these reasons, wide usage of ENO/WENO in application is limited.

One alternative is the artificial viscosity. With adding an artificial diffusion term to the governing equation, the pseudo oscillations at discontinuities are detected and smoothed out.

In the smooth region, the artificial viscosity is set to zero. This strategy was first brought up by Persson and Peraire [19] for discontinuous Galerkin method and then extended to the FR/CPR method in [71]. It has good properties in accuracy preservation and convergence. However, the time step for stability is highly limited when explicit time-stepping schemes is used due to the diffusion operator. The fine tuning of the free parameters is problem dependent. And we found that for relatively high Reynolds number flow problems, this method is not always robust.

Limiter is another option for dealing with discontinuities. There are many different limiters. For high-order method, Scott et al presented a limiter for discontinuous Galerkin methods in [72]. However, like most limiters' issue, for steady problems with shocks, it is not able to converge. Michalak and Gooch proposed an accuracy preserving limiter for high-order finite volume schemes in [73]. It introduced a smooth function as an alternative for the minimum function to maintain monotonicity and good convergence. It also use a smooth indicator to eliminate the limiting process in smooth regions to achieve high-order accurate solutions. Inspired by this limiter, we propose a new limiter for the FR/CPR scheme which works for the discontinuous finite element catalog methods better.

4.1 High-order Flux Limiting

In this section, each and every requirements of the limiter are discussed. At the end, the completed algorithm of the limiter is given.

4.1.1 Limiting Function Φ

In FR/CPR, as introduced in the last section, solution in each cell is a polynomial.

$$u_i(x) = \sum_{j=1}^{N} u_{i,j} L_{i,j}(x). \tag{4.1}$$

The solution at FPs are reconstructed from the polynomial,

$$u_{i,fp} = \sum_{j=1}^{N} u_{i,j} L_{i,j}(x_{i,fp}). \tag{4.2}$$

The reconstructed solution at flux points at discontinuities may overshoot due to the pseudo oscillations of high-order methods. To stabilize the simulation, we need to limit the solution at flux points in some range. Here we use $[min(\bar{u}_i^{neighbor}), max(\bar{u}_i^{neighbor})]$, where $\bar{u}_i^{neighbor}$ is the average solution in the direct face neighboring cells of cell i, including i itself. Let us use $u_{i,fp} > max(\bar{u}_i^{neighbor})$ for instance. Define $y = \frac{max(\bar{u}_i^{neighbor}) - \bar{u}_i}{u_{i,fp} - \bar{u}_i}$. A minmod style limiter would use the function

$$u_{i,fp} = \bar{u}_i + \Phi_i(1, y)(u_{i,fp} - \bar{u}_i). \tag{4.3}$$

where

$$\Phi_i(1, y) = min(1, y) = \begin{cases} y, & y < 1 \\ 1, & y \geq 1 \end{cases} \tag{4.4}$$

This function is not differentiable. When used together with high order schemes, it destroys the high order accuracy and the convergence for steady problems. Michalak and Gooch [73] introduced another function which is differentiable and close to the min function. It smoothly connect y and 1 without the sudden jump at 1. We extend the function to a more general definition.

$$\Phi_i(1, y) = \tilde{min}(1, y) = \begin{cases} P(y), & y < y_t \\ 1, & y \geq y_t \end{cases} \tag{4.5}$$

where $P(y)$ is a polynomial satisfying

$$P \mid_{y_0} = y_0, P \mid_{y_t} = 1, \frac{dP}{dy} \mid_{y_0} = 1, \frac{dP}{dy} \mid_{y_t} = 1, P(y) \leq min(1, y), y \in [y_0, y_t] \tag{4.6}$$

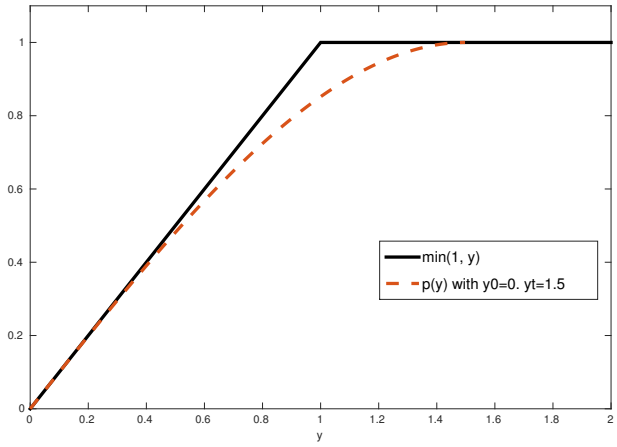

Figure 4.1: $\tilde{min}(1, y)$ with $y_0 = 0.$, $y_t = 1.5$ and $min(1, y)$

The resulting cubic polynomial for $y_0 = 0., y_t = 1.5$ is

$$P(y) = -\frac{4}{27}y^3 + y, \tag{4.7}$$

and is plotted in Figure 4.1. This function is critical in preserving the high order accuracy and convergence for steady problems.

4.1.2 Smooth Region Correction

With the new function, the overshooting of the solution at discontinuities is limited. However, in the smooth regions, the solution may also be limited. To maintain high order accuracy and good convergence, it is also essential to permit overshooting in the smooth area, such as the turbulence region in a shock and turbulence interaction problem. To make a smooth connection between fully limiting the solution and completely not limiting the solution, we

introduce σ,

$$\sigma = \begin{cases} 1, & S_i \leq S_0 - \kappa \\ \frac{1}{2}(1 - sin(\frac{1}{2}\pi\frac{S_e - S_0}{\kappa})), & S_0 - \kappa < S_i < S_0 + \kappa \\ 0, & S_i \geq S_0 + \kappa \end{cases} \tag{4.8}$$

where S_i is the smooth indicator[19], $\kappa = 4$. As the solution in current cell is given in Eq. 4.1, we consider a truncated expansion of the same solution containing the terms up to order $p-1$,

$$\hat{u} = \sum_{j=1}^{N(p-1)} u_j L_j. \tag{4.9}$$

Within each element Ω_i, the discontinuity sensor is defined as

$$S_i = \frac{\langle u - \hat{u}, u - \hat{u} \rangle_i}{\langle u, u \rangle_i}, \tag{4.10}$$

where $(\cdot, \cdot)_i$ is the standard inner product. Our final limiter function turn into

$$\tilde{\Phi}_i = \sigma_i + (1 - \sigma_i)\Phi_i. \tag{4.11}$$

4.1.3 Convergence Property

The iterative convergence has been an issue for limiters, especially for the finite element style high-order methods. We propose a new way to monitor the simulation history. Instead of monitoring the residual of each step n, we monitor $\frac{u^n - u^{n-1}}{\Delta t}$. For smooth problems, these two are identical. But for discontinuous problems with a limiter, the solution is limited every step, making the residual hang at a relatively high level. Adding the residual's influence to the solution only makes it to go back to the solution with overshooting. The whole process repeats with the residual staying high but the solution change rate decrease. We are going to show this later in the result of steady problem.

4.1.4 Completed Algorithm

The limiter process discussed above is very easy to implemented in a current high-order solver. In this section, we give the complete algorithm for applying the limiter to the reconstruction for each flow property of each element i.

a. Compute the element average of the solution for all elements and find the maximum and minimum averaged solution in each elements neighbors, including the element itself.

b. Compute the unlimited solution at flux point using reconstruction.

c. Compute Φ_i using equation 4.5 for each flux point and choose the minimum value.

d. Compute discontinuity detector S_e using equation 4.10 and σ_i using equation 4.8.

e. Compute $\tilde{\Phi}$ using equation 4.11

f. Limit the solution using equation 4.3 with $\tilde{\Phi}_i$ replacing Φ_i.

4.2 Numerical Results

4.2.1 1D Sod Shock Tube Problem

Sod shock tube problem is a common test case for the accuracy of the numerical method. The initial profile is given as follow:

$$(\rho_L, u_L, p_L) = (1.0, 0.0, 1.0)(\rho_R, u_R, p_R) = (0.125, 0.0, 0.1) \tag{4.12}$$

The computational domain is $[0, 1]$, and is tessellated with 100, 200 and 400 elements. The interface is initially located at $x = 0.5$. Simulation is carried out till t=0.2.

The density distribution computed with CPR-P2 and the new flux limiter is shown in Figure4.2. The flux limiter effectively stabilizes the simulation. We can see that at relatively low resolution, say 100 cells, oscillations exist at the expansion wave and the shocks. With the increase of the resolution, the solution converges to the exact solution. This 1D test

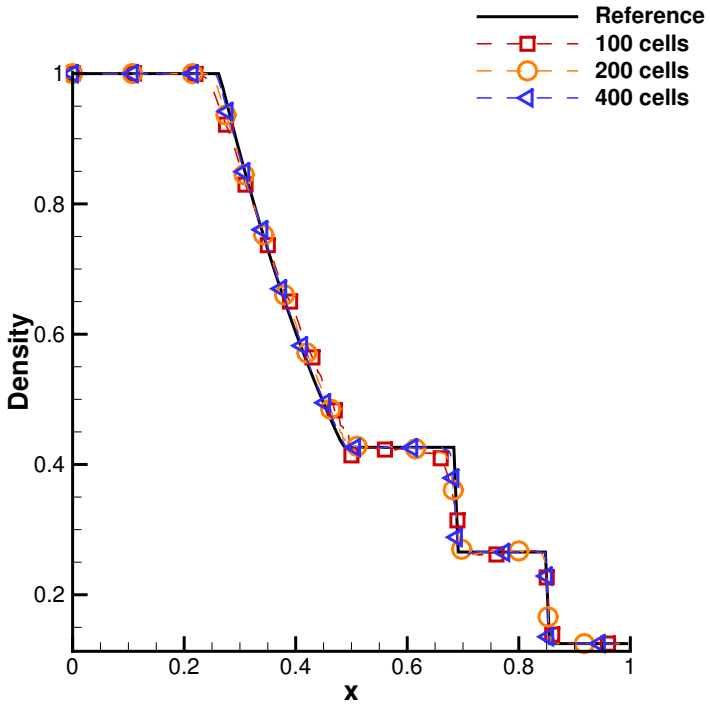

Figure 4.2: Density distribution at $t = 0.2s$

proves that the flux limiter gives correct solution.

4.2.2 Supersonic Flow in A Convergent Channel with A Ramp on the Floor

This test case is ideal for testing the limiter working with high-order Euler solver. The channel consists of a 15° compression ramp followed by a 15° expansion corner along the lower and upper walls as shown in Fig. 4.3. The inlet flow is supersonic with an Mach number of 2.0. Due to the symmetric geometry, only the flow in the lower half of the channel is studied. The gird we used has 96×32 cells and is shown in Fig.4.4.

The Mach number flood contours in the channel for CPR-P2 is presented in Fig. 4.5, 4.6 and 4.7. Very sharp shocks are captured. The limiter for the $P2$ case $\tilde{\Phi}$ is plotted in Fig. 4.8. We observe that only the cells with discontinuities are limited, $\tilde{\Phi} \neq 1$. The smooth regions

are not limited, $\tilde{\Phi} = 1$. It is worth noting that in the limited cells, the value of $\tilde{\Phi}$ is very close to 1, meaning that just appropriate amount of limiting is added so that the simulation is stabilized while the high order solution is very little damaged. Fig.4.9 shows the convergence history. We can see that with the *res* hanging at 10^{-2}, $\frac{dq}{dt}$ was able to converge to machine zero.

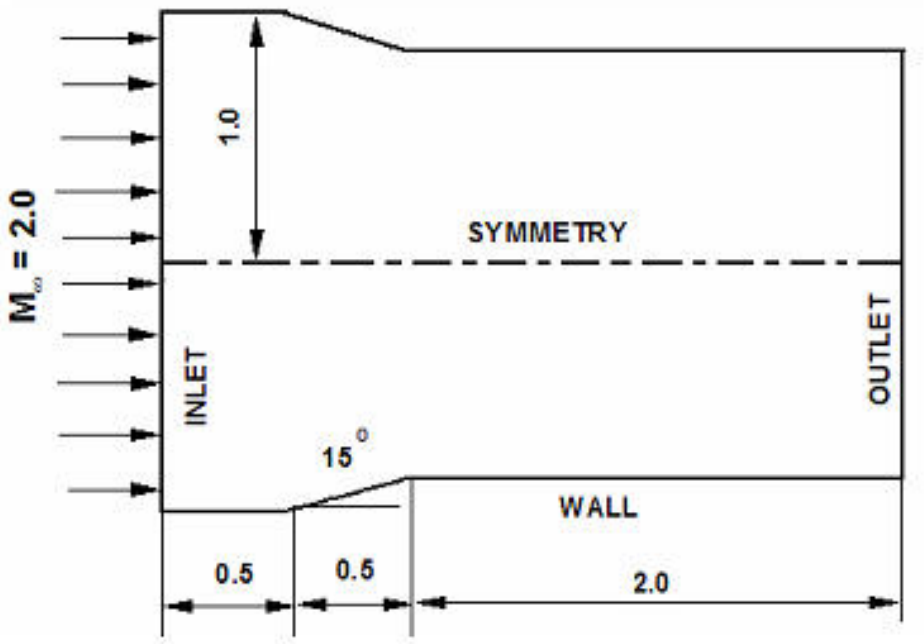

Figure 4.3: Geometry of the channel

4.2.3 Transonic Flow over a NACA0012 Airfoil

The transonic steady case was studied. The Mach number is set as 0.8 and the angle of attack is 1.25^o. A r^{th} order mesh is generated and used in this study, which is shown in Figure 4.10. Specifically, the far field boundary is of 1000 chord length away from the airfoil. The mach contour and the limiting function contour of the simulation with CPR-P2 are shown in Figure 4.11 and 4.12. The simulation converged to machine zero.

From the contour, we see the limiting is precisely added to the cells that has disconti-

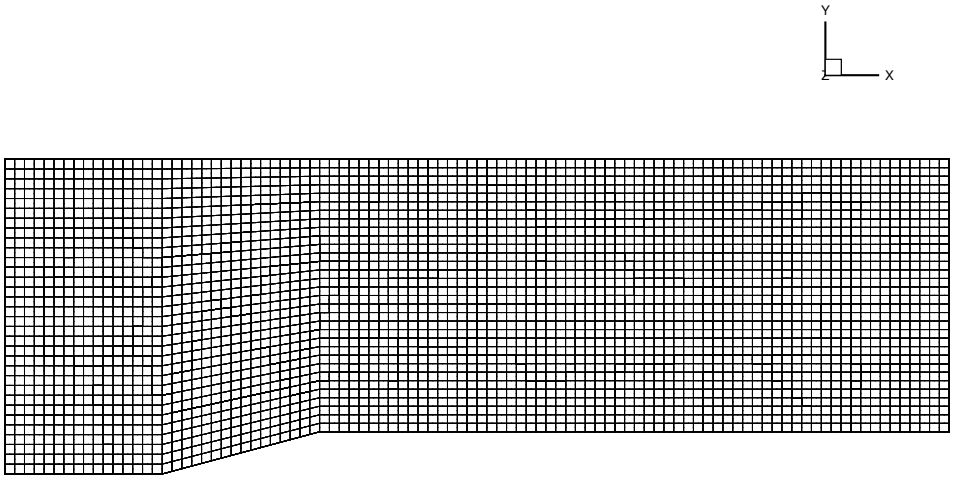

Figure 4.4: Mesh of the channel

nuities. However, again, from the plot of $Mach$, we see the unnecessary oscillations behind the shock. This could be due to the over limiting in the smooth region. More study about removing the oscillations is definitely worth doing.

4.2.4 Shock-isentropic Vortex Interaction

This test case is the interaction between a stationary shock wave and an isentropic vortex convection[74]. The computational domain is $[0, 2] \times [0, 1]$, discretized using uniform cells with size of $1/100 \times 1/100$, shown in Fig.4.13. A stationary shock with a pre-shock Mach number of $M_s = 1.1$ is positioned at $x = 0.5$. The upstream state is $(\rho_L, u_L, v_L, p_L) = (1.0, M_s\sqrt{\gamma}, 0.0, 1.0)$. The right quantities are calculated from the left ones using jump conditions. An isentropic vortex is superposed to the flow left to the shock and centers at $(x_c, y_c) = (0.25, 0.5)$ with the following flow conditions:

$$v_\theta = \epsilon\tau e^{\alpha(1-\tau^2)}, \rho = (1 - \frac{\gamma - 1}{4\alpha\gamma}\epsilon^2 e^{2\alpha(1-\tau^2)})^{\frac{1}{\gamma-1}}, p = \rho^\gamma, \tag{4.13}$$

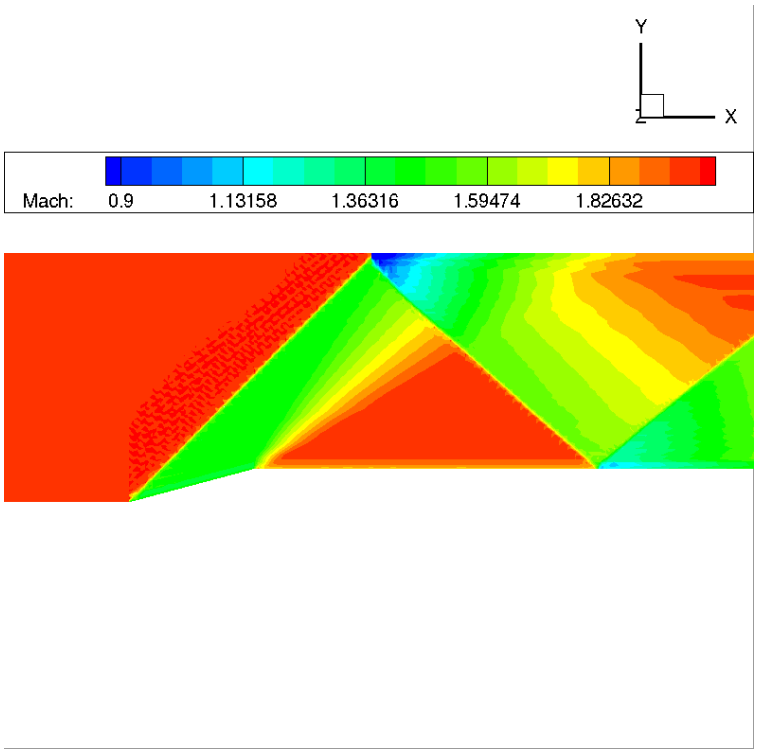

Figure 4.5: Contour of $Mach$ number for CPR-P2

with $\tau = r/r_c$ and $r = \sqrt{(x - x_c)^2 + (y - y_c)^2}$. Here, v_θ is the circumferential velocity, ϵ is the strength of the vortex, α is the decay rate of the vortex, and r_c is the critical radius for which the vortex has the maximum strength. In the present study, $\epsilon = 0.3, \alpha = -.204, r_c = 0.05$. The simulations is carried out till $t = 0.8s$.

Fig.4.14, 4.15 and 4.16 show the pressure contour. We can see that the shock is sharply captured while the vortex is very accurately resolved. The limiter $\tilde{\Phi}$ for p2 case is shown in Fig.4.17. It is clear that only the narrow line of shock is limited. The vortex is not bothered at all. This result proves that this limiter is able to handle vortex shock interaction by precisely stabilizing the oscillation at discontinuity without doing harm to the resolution of the smooth vortex region. This is a positive sign for the using of this limiter in the challenging shock and turbulence interactions. However, we should pay attention to the weak oscillations on the results from higher order schemes. Those oscillations didn't influence the stability of the simulation. But the study of removing those oscillations is needed in the future.

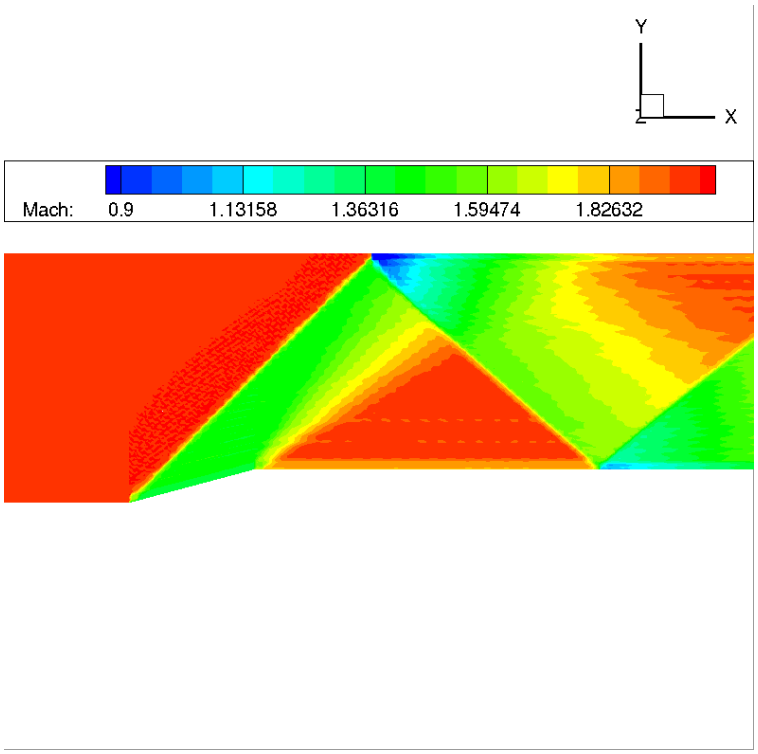

Figure 4.6: Contour of $Mach$ number for CPR-P3

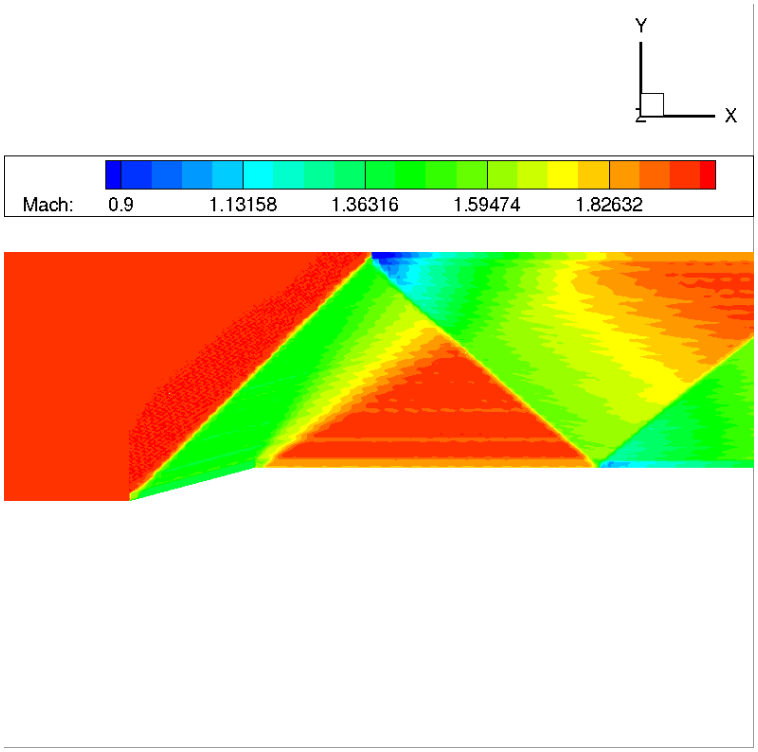

Figure 4.7: Contour of $Mach$ number for CPR-P4

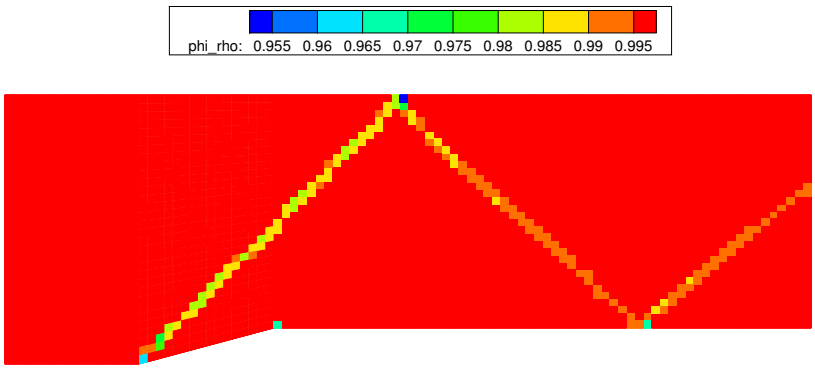

Figure 4.8: Contour of $\tilde{\Phi}_\rho$ for CPR-P2

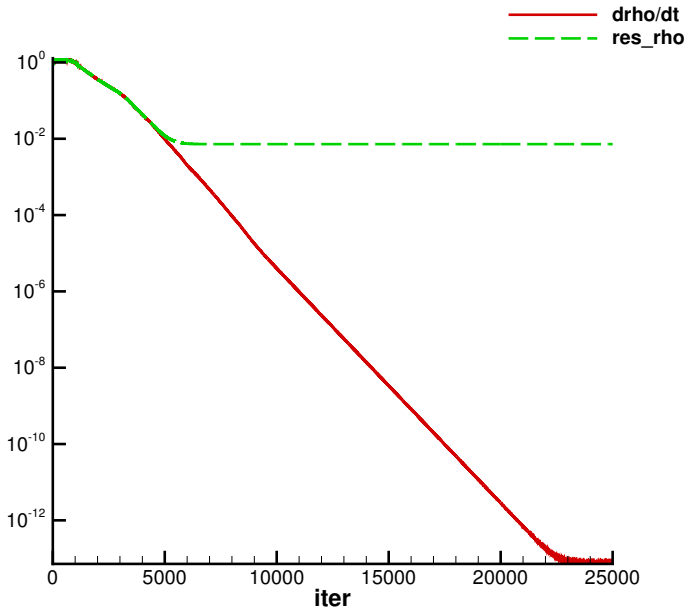

Figure 4.9: Residual and solution change rate for CPR-P2

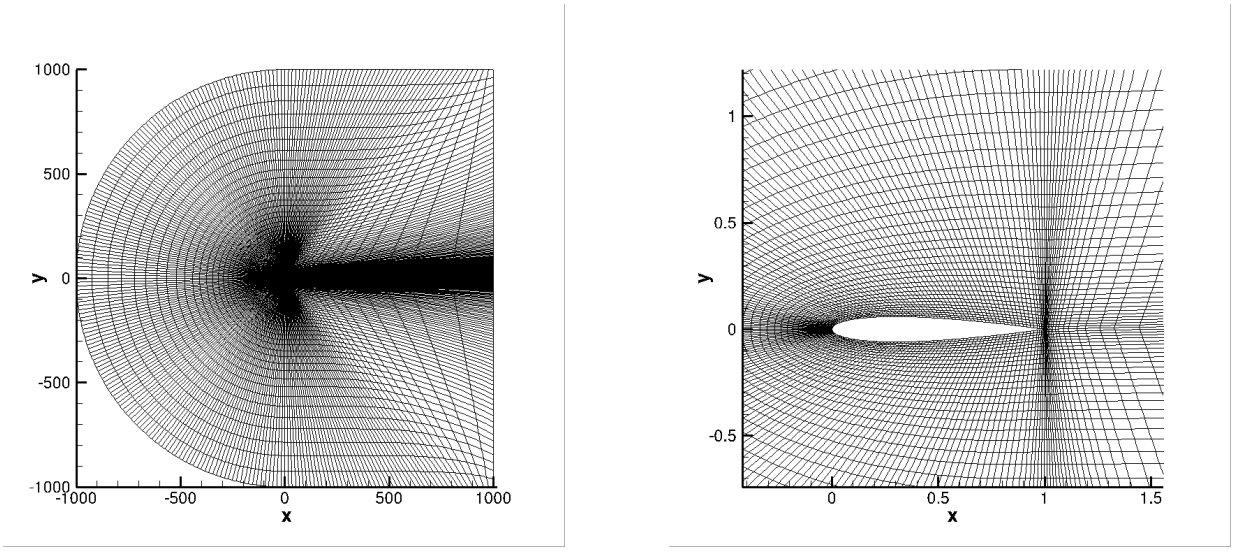

(a) (b)

Figure 4.10: Grid for NACA0012

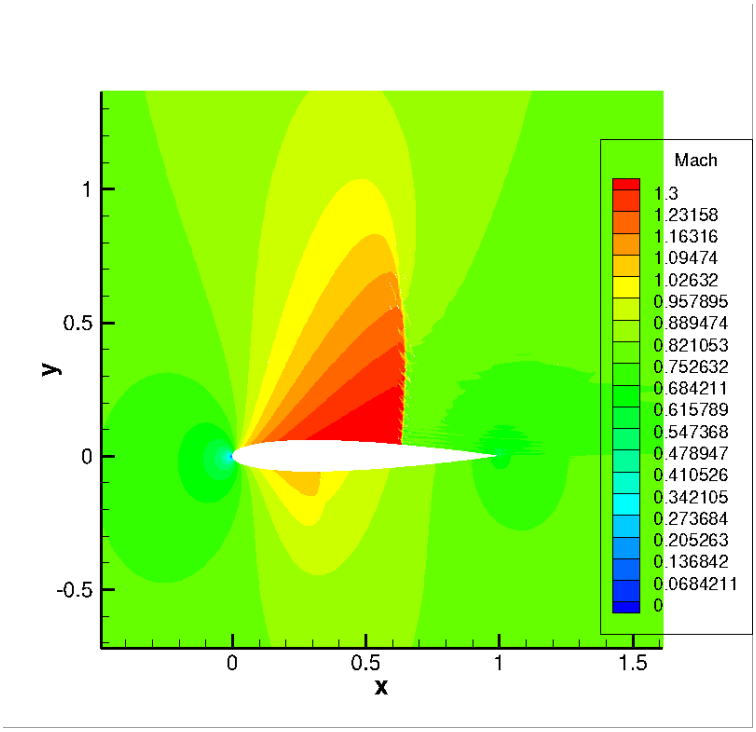

Figure 4.11: *Mach* contour computed with CPR-P2

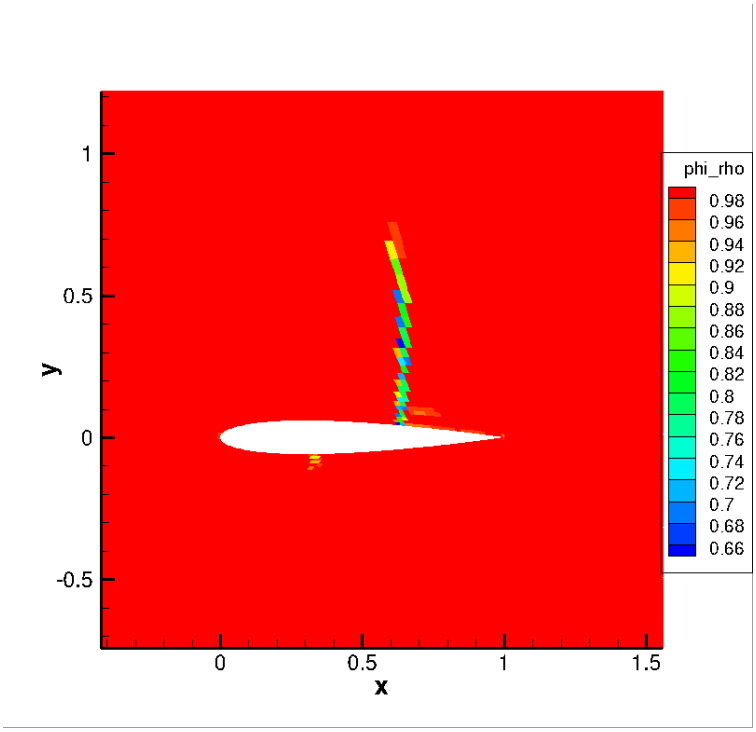

Figure 4.12: Φ contour computed with CPR-P2

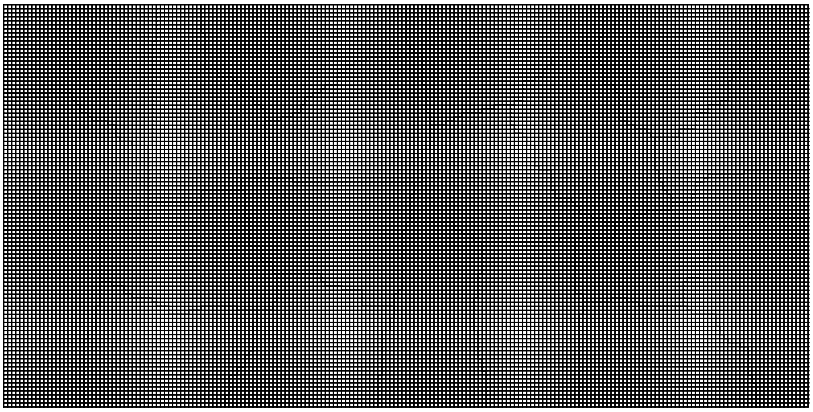

Figure 4.13: Mesh for shock and vertex interaction

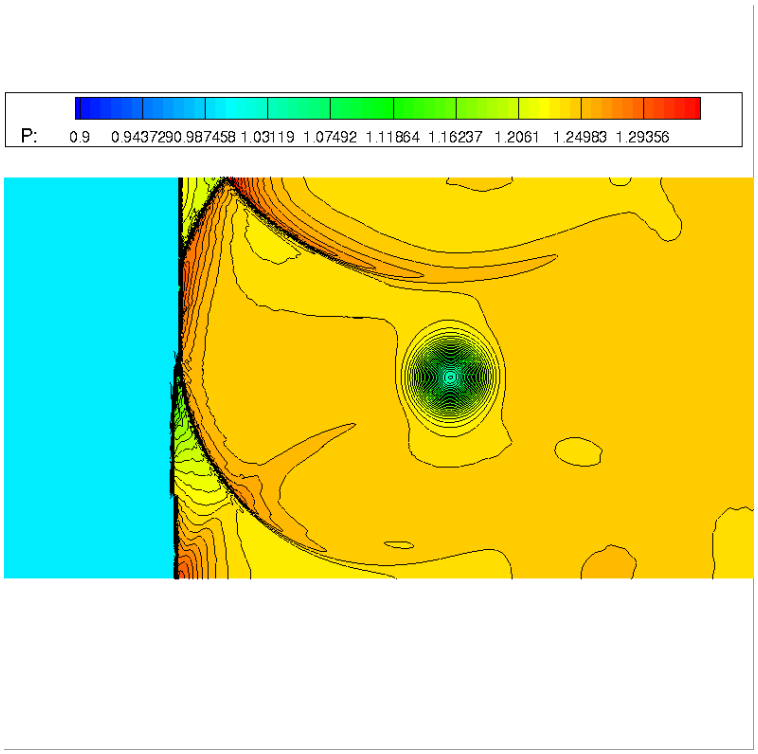

Figure 4.14: Pressure contour for CPR-P2

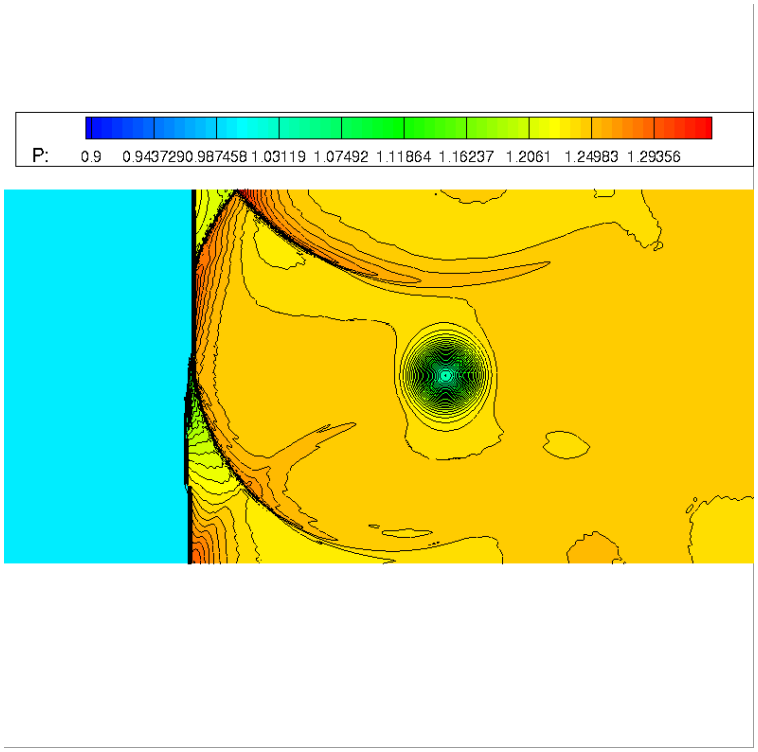

Figure 4.15: Pressure contour for CPR-P3

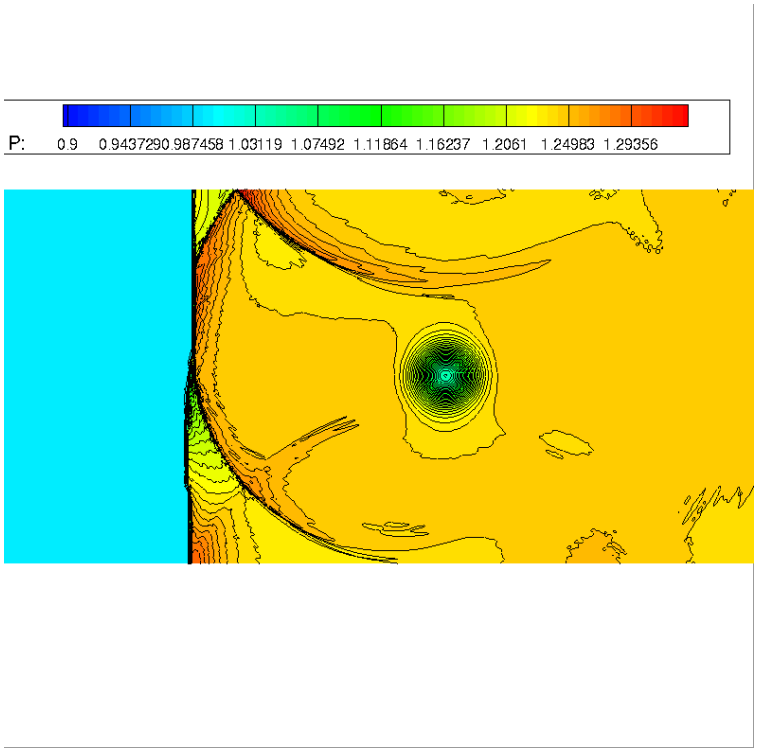

Figure 4.16: Pressure contour for CPR-P4

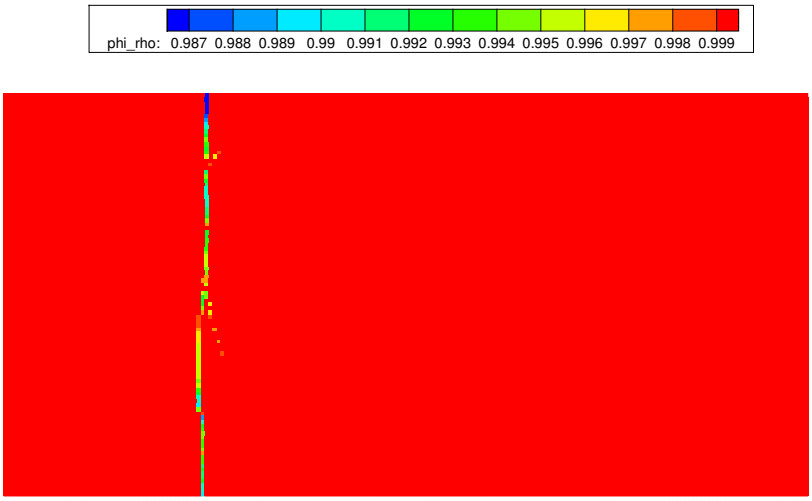

Figure 4.17: Contour of $\tilde{\Phi}_\rho$ for CPR-P2

Chapter 5

Conclusions

5.1 Conclusions

In the present study, five SGS models are evaluated with the 1D Burgers' equation discretized with the CPR method. Different LES cell sizes were tested with a fixed filter width. In both the a priori and a posteriori tests on a fine LES mesh, the SSM and the MM showed excellent correlation with the true SGS, while the other models do not predict the SGS stress satisfactorily. However, as the LES cell size increases, numerical truncation error is dominant in the results. In this case, none of the models shows any benefits over ILES.

The analysis of scale similarity shows that perfect scale similarity exists for arbitrary (periodic) data including turbulence under the assumption that the spectrum contains relatively low frequency contents with respect to the filter width, regardless of amplitude and phase angle of each mode. In an actual large eddy simulation, in which both large and sub-grid scales exist, the present result on the ratio of the resolved scale stress and the SGS stress may be the upper limit. Test results with data including higher modes near the grid cutoff demonstrate that there is a high level of correlation between the modelled and SGS stresses. Furthermore, $\gamma = 1$ demonstrates consistently higher correlation coefficients than $\gamma = 2$. This may indicate that $\gamma = 1$ is preferred in a SSM implementation. The stability of the

SSM is also investigated. The study shows that it is the central flux rather than the SSM that causes energy accumulating at high frequencies, which may lead to the instability of a simulation. In this case, extra dissipation other than SSM, the DS, for example, is necessary. However, the schemes with upwind flux smoothly damps out the energy at high frequencies. Thus no extra dissipation is needed to stabilize the simulation with the SSM.

The new shock capturing limiter has shown its good properties. Simulations of steady problems is able to converge with the new limiter. For unsteady problems, it shows that accuracy is preserved at the smooth regions while the shock is effectively stabilized.

ILES with the new limiter has been successfully applied to industry high Reynolds number transonic turbulent flow and showed good comparison results with experiments.

5.2 Future work

Several potential areas of future work are identified during the course of this work:

- Further study of the limiter to make it work generally for supersonic turbulent flow
- Implement the time-accurate local time stepping method for extreme scale LES of turbulent flow
- Improve and test the wall model for more complicated wall-bounded turbulent flows

References

[1] H. T. Huynh. A flux reconstruction approach to high-order schemes including discontinuous Galerkin methods. *AIAA Paper 2007-4079*, 2007.

[2] Z. J. Wang and H. Gao. A unifying lifting collocation penalty formulation including the discontinuous Galerkin, spectral volume/difference methods for conservation laws on mixed grids. *Journal of Computational Physics*, 228:8161–8186, 2009.

[3] Z. J. Wang, H. Gao, and T. Haga. A unifying discontinuous formulation for hybrid meshes. *Adaptive High-Order Methods in Computational Fluid Dynamics*, pages 423–453, 2011.

[4] Chunlei Liang, Christopher Cox, and Michael Plesniak. A comparison of computational efficiencies of spectral difference method and correction procedure via reconstruction. *Journal of Computational Physics*, 239(0):138 – 146, 2013.

[5] Georgialdis NJ, Rizzetta DP, and Fureby C. Large-eddy simulation:current capabilities, recommended practices, and future research. *AIAA J*, pages 31772–1784, 2010.

[6] Smagorinsky J. General circulation experiments with the primitive equations. *The basic experiment, Weather Rev*, pages 91–99, 1963.

[7] Lilly DK. A propose modification of the germano subgrid-sclae closure method. *Phys. Fluids*, A 4:633–635, 1992.

[8] Germano M, Piomelli U, Moin P, and Cabot WH. A dynamic subgrid-scale eddy viscosity model. A 3:1760–1765, 1991.

[9] Bardina J, Ferziger JH, and Reynolds WC. Improved subgrid scale models for large eddy simulation. *Am. Inst. Aeronaut. Astronaut*, pages 80–1357, 1980.

[10] Harish Gopalan and Stefan Heinz. A unified rans-les model:computational development, accuracy and cost. *J. Computational Physics*, 249:249–274, 2013.

[11] Piomelli U and Liu J. Large-eddy simulation of rotating channel flows using a localized dynamic model. *Phys.Fluids*, 7:839–848, 1995.

[12] Ghosal S and Rogers MM. A numerical study of self-similarity in a turbulent plane wake using large-eddy simulation. *Phys. Fluids*, 9:1729–1739, 1997.

[13] Akselvoll K and Moin P. Large-eddy simulation of turbulent confined coannular jets. *J. Fluid Mech*, 315:387–411, 1996.

[14] Wu X and Squires KD. Large eddy simulation of an equilibrium three dimensional turbulent boundary layer. *Am. Inst. Aeronaut. Astronaut. J.*, 35:67–74, 1997.

[15] Akselvoll K and Moin P. Large-eddy simulation of turbulent confined coannular jets. *J Fluid Mech*, pages 315:387–411, 2010.

[16] Meneveau C and Katz J. Scale-invariance and turbulence models for large-eddy simulation. *Annu. Rev. Fluid Mech.*, pages 1–32, 2000.

[17] Durbin P. A and Pettersson Reif B. A. *Statistical Theory and Modeling for Turbulent Flows*. A John Wiley and Sons, 2011.

[18] Grinstein F. F. and Margolin L. G. *Implicit large eddy simulation:computing turbulent fluid dynamics*. Cambridge University Press, 2011.

[19] P. O Persson and J. Peraire. Sub-cell shock capturing for discontinuous galerkin methods. *AIAA Conference*, page 112, 2006.

[20] Garret E. Barter and David L. Darmofal. Shock capturing with higher-order, pde-based artificial viscosity. *AIAA Conference*, page 3823, 2007.

[21] C.-W. Shu. Essentially non-oscillatory and weighted essentially non-oscillatory schemes for hyperbolic conservation laws. Technical report, 1997.

[22] C.-W. Shu. High order finite difference and finite volume weno schemes and discontinuous galerkin methods for cfd. Technical report, 2001.

[23] B. Cockburn, F. Li, and C. W. Shu. Locally divergence-free discontinuous galerkin methods for the maxwell equations. *Journal of Computational Physics*, pages 588–610, 2004.

[24] M. K. Kadalbajoo and K. C. Patidar. Exponentially fitted spline in compression for the numerical solution of singular perturbation problems. *Computers and Mathematics with Applications*, page 751, 2003.

[25] Y. N. Reddy and P. P. Chakravarthy. An exponentially fitted finite difference method for singular perturbation problems. *Applied Mathematics and Computation*, page 83, 2004.

[26] S. Christofi. *The study of building blocks for essentially non-oscillatory (ENO) schemes*. PhD thesis, Brown University, 1996.

[27] L. Yuan and C. W. Shu. Discontinuous galerkin method based on non-polynomial approximation spaces. *J. Comp. Phys.*, pages 295–323, 2006.

[28] Y. G and Li. Wavenumber-extended high-order upwind-biased finite-difference schemes for convective scalar transport. *Journal of Computational Physics*, pages 133–225, 1997.

[29] H. Q. Sia and T. G. Wangb. Grid-optimized upwind dispersion-relation-preserving scheme on non-uniform cartesian grids for computational aeroacoustics. *Aerspace Science and Technology*, pages 608–617, 2008.

[30] C. K. W. Tam. Computational aeroacoustics: Issues and methods. *AIAA Journal*, pages 1788–1796, 1995.

[31] C. K. W. Tam and J. C. Webb. Dispersion-relation-preserving finite difference schemes for computational acoustics. *J. Comp. Phys.*, pages 262–281, 1993.

[32] M. Zhuang and R. F. Chen. Optimized upwind dispersion relations preserving finite difference scheme for computational aeroacoustics. *AIAA Journal*, page 11, 1998.

[33] M. Zhuang and R. F. Chen. Application of high-order optimized upwind schemes for computational aeracoustics. *AIAA Journal*, page 3, 2002.

[34] Yi Li and Z. J. Wang. An optimized correction procedure via reconstruction formulation for broadband wave computation. *Commun. Comput. Phys.*, pages 1265–1291, 2013.

[35] C. K. W. Tam and J. C. Webb. Dispersion-relation-preserving finite difference schemes for computational acoustics. *Journal of Computational Physics*, pages 262–281, 1993.

[36] M. Zhuang and R. F. Chen. Optimized upwind dispersion relation preserving finite difference scheme for computational aeroacoustics. *AIAA Journal*, page 11, 1998.

[37] Y.Li and Z. J. Wang. A priori and a posteriori evaluations of sub-grid scale models with the burgers' equation. *AIAA Paper 2015-1283*, 2015.

[38] Moin P and Kim J. Numerical investigation of turbulent channel flow. *J. Fluid Mech*, 118:341–77, 1982.

[39] Rogallo RS and Moin P. Numerical simulation of turbulent flows. *Annu. Rev. Fluid Mech*, 16:99–137, 1984.

[40] Lesieur M and Metais O. New trends in large-eddy simulations of turbulence. *Annu. Rev. Fluid Mech*, 16:99–137, 1984.

[41] Pope SB. *Turbulent Flows*. Cambridge Univ. Press, Cambridge UK.

[42] Clark RA, Ferziger JH, and Reynolds WC. Evaluation of subgrid-scale models using an accurately simulated turbulent flow. *J.Fluid Mech*, 91:1–16, 1979.

[43] McMillan OJ, Ferzinger JH, and Rogallo RS. Tests of new subgrid scale models in strained turbulence. *Am. Inst. Aeronaut. Astronaut.*, 80:13–39, 1980.

[44] Ghosal S and Lund TS. A dynamic localization model for large eddy simulation of turbulent flows. *J. Fluid Mech*, 286:229–255, 1995.

[45] Liu S and Meneveau C. On the properties of similarity subgrid-scale models as deduced from measurements in a turbulent jet. *J. Fluid Mech*, 275:83–119, 1994.

[46] Akhavan R, Ansari A, and Kang S. Subgrid-scale interactions in a numerically simulated planar turbulent jet and implications for modeling. *J. Fluid Mech.*, 408:83–120, 2000.

[47] Z.J. Wang and Y.Li. An analysis of scale similarity and its implications for large eddy simulation. *Commun. Comput. Phys.*, 2016. Accepted.

[48] Zan Y and Street RL. A dynamic mixed subgrid-scale model and its application to turbulent recirculating flows. *Phys Fluids*, page A 5 3186, 1993.

[49] Wu X and Squires KD. Numerical investigation of the turbulent boundary layer over a bump. *J. Fluid Mech.*, 362:229–271, 1998.

[50] Vreman B and Geurts B. On the formulation fo the dynamic mixed subgrid-scale model. *Phys Fluids*, pages 6:4057–9, 1994.

[51] H. Gao T. Haga and Z. J. Wang. A high-order unifying discontinuous formulation for the Navier-Stokes equations on 3D mixed grids. *Math. Model. Nat. Phenom.*, 6(03):28–56, 2011.

[52] H. Gao and Z. J. Wang. A conservative correction procedure via reconstruction formulation with the chain-rule divergence evaluation. *Journal of Computational Physics*, 232:7–13, January 2013.

[53] H. Gao and Z. J. Wang. Differential formulation of discontinuous Galerkin and related methods for the Navier-Stokes equations. *Commun. Comput. Phys.*, 13:1013–1044, 2013.

[54] L. Shi and Z. J. Wang. Adjoint-based Error Estimation and Mesh Adaptation for the Correction Procedure via Reconstruction Method. *Journal of Computational Physics*, 295:261–284, 2015.

[55] Lei Shi and Z. J. Wang. Adjoint based anisotropic mesh adaptation for the cpr method. *AIAA Paper 2013-2869*, 2013.

[56] Meilin Yu, Z. J. Wang, and Yen Liu. On the accuracy and efficiency of discontinuous Galerkin, spectral difference and correction procedure via reconstruction methods. *Journal of Computational Physics*, 259:70–95, 2014.

[57] Yanan Li and Z. J. Wang. Evaluation of optimized CPR schemes for computational aeroacoustics benchmark problems. *AIAA Paper 2013-2689*, 2013.

[58] F. Bassi and S. Rebay. Gmres discontinuous Galerkin solution of the compressible Navier-Stokes equations. *Lecture Notes in Computational Science and Engineering*, 11:197–208, 2000.

[59] Sigal Gottlieb and Chi-Wang Shu. Strong stability-preserving high-order time discretization methods. *Scociety for Industrial and Applied Mathematics*, 43:89–112, 2011.

[60] Fureby C and Tabor G. A comparative sutdy of subgrid-scale models in homogeneous isotropic turbulence. *Phys. Fluids*, pages 9:1416–29, 1997.

[61] Erlebacher G and Hussaini MY. Toward the large-eddy simulation of compressible turbulent flows. *J. Fluid Mech.*, pages 238:155–85, 1992.

[62] Jaberi FA and James S. A dynamic similarity model for large eddy simulation of turbulent combustion. *Phys. Fluids*, pages 10:1775–77, 1998.

[63] Sarghini F and Piomelli U. Scale similar models for large-eddy simulations. *Phys. Fluids*, 11:1596–1607, 1999.

[64] Speziale CG. Galilean invariance of subgrid-scale stress models in les of turbulence. *J. Fluid Mech*, 275:55–62, 1985.

[65] Cook AW. Determination of the constant coefficient in scale similarit models of turbulence. *Phys Fluids*, pages 9:1485–87, 1997.

[66] Cook AW. Determination of the constant coefficient in scale similarity models of turbulence. *Phys. Fluids*, 9:1485–1487, 1997.

[67] R. Abgrall. On essentially non-oscillatory schemes on unstructured meshes: analysis and implementation. *J. Comp. Phys.*, pages 45–58, 1994.

[68] C. W. Shu and T. A. Zang. High-order eno schemes applied to two- and three-dimensional compressible flow. *Applied Numerical Mathematics*, pages 9:45–71, 1992.

[69] O. Friedrich. Weighted essentially non-oscillatory schemes for the interpolation of mean values on unstructured grids. *J. Comp. Phys.*, pages 194–212, 1998.

[70] C. Q. Hu and C. W. Shu. Weighted essentially non-oscillatory schemes on triangular meshes. *J. Comp. Phys.*, pages 97–127, 1999.

[71] Melin Yu and Z. J. Wang. Shock capturing for correction procedure via reconstruction methods using artificial viscosity and diffusivity. *ICCFD8*, page 8, 2014.

[72] Scott A. Moe and James A. Rossmanith. A simple and effective high-order shock-capturing limiter for discontinuous galerkin methods. *Math. NA*, page 1, 2015.

[73] Christopher Michalak and Carl Ollivier-Gooch. Accuracy preserving limiter for the high-order accurate solution of the euler equations. *Journal of Computational Physics*, pages 8693–8711, 2009.

[74] G. S. Jiang and C. W. Shu. Efficient implementation of weighted eno schemes. *J. Comp. Phys.*, pages 202–228, 1996.